Biophysical Journal
Article

Biophysical Society

Stochastic Model of T Cell Repolarization during Target Elimination I

Ivan Hornak[1] and Heiko Rieger[1,*]
[1]Center for Biophysics (ZBP) and Department of Theoretical Physics, Saarland University, Saarbrücken, Germany

ABSTRACT Cytotoxic T lymphocytes (T) and natural killer cells are the main cytotoxic killer cells of the human body to eliminate pathogen-infected or tumorigenic cells (i.e., target cells). Once a natural killer or T cell has identified a target cell, they form a tight contact zone, the immunological synapse (IS). One then observes a repolarization of the cell involving the rotation of the microtubule (MT) cytoskeleton and a movement of the MT organizing center (MTOC) to a position that is just underneath the plasma membrane at the center of the IS. Concomitantly, a massive relocation of organelles attached to MTs is observed, including the Golgi apparatus, lytic granules, and mitochondria. Because the mechanism of this relocation is still elusive, we devise a theoretical model for the molecular-motor-driven motion of the MT cytoskeleton confined between plasma membrane and nucleus during T cell polarization. We analyze different scenarios currently discussed in the literature, the cortical sliding and capture-shrinkage mechanisms, and compare quantitative predictions about the spatiotemporal evolution of MTOC position and MT cytoskeleton morphology with experimental observations. The model predicts the experimentally observed biphasic nature of the repositioning due to an interplay between MT cytoskeleton geometry and motor forces and confirms the dominance of the capture-shrinkage over the cortical sliding mechanism when the MTOC and IS are initially diametrically opposed. We also find that the two mechanisms act synergistically, thereby reducing the resources necessary for repositioning. Moreover, it turns out that the localization of dyneins in the peripheral supramolecular activation cluster facilitates their interaction with the MTs. Our model also opens a way to infer details of the dynein distribution from the experimentally observed features of the MT cytoskeleton dynamics. In a subsequent publication, we will address the issue of general initial configurations and situations in which the T cell established two ISs.

SIGNIFICANCE Cytotoxic T lymphocytes are the main cytotoxic killer cells of the human body to eliminate target cells. The microtubule (MT) organizing center repositioning plays a key role in the killing process, and two underlying mechanisms are discussed: cortical sliding and capture-shrinkage. We devise a theoretical model for the molecular-motor-driven motion of the MT cytoskeleton confined between the membrane and the nucleus during T cell polarization and make quantitative predictions about the spatiotemporal evolution of the MT organizing center position and the MT cytoskeleton morphology comparable with experiments. It reveals the mechanism underlying the experimentally observed biphasic behavior and a remarkable synergy between capture-shrinkage and cortical sliding mechanisms. It also opens a way to infer dynein distribution from details of MT cytoskeleton dynamics.

INTRODUCTION

Cytotoxic T lymphocytes and natural killer (NK) cells have a key role in our immune system by finding and destruction of virus-infected and tumor cells, parasites, and foreign invaders. Once a T cell leaves the thymus, it circulates through the organism in search of a target cell. The directional killing of a target cell is completed in three subsequent steps. First, T cell receptors bind to antigens on the surface of the target cell presented by the major histocompatibility complex (1–6), leading to the creation of a tight contact zone called the immunological synapse (IS) (7–9) composed of multiple supramolecular activation clusters (9–11). In the second step, the cell repolarizes by relocating the microtubule organizing center (MTOC) toward the IS (12–18) under the influence of forces exerted on MTs. Moreover, because mitochondria, the Golgi apparatus, and the endoplasmic reticulum are attached to MTs, these organelles are dragged along with the MT cytoskeleton

Submitted October 28, 2019, and accepted for publication January 30, 2020.

*Correspondence: h.rieger@physik.uni-saarland.de

Editor: Kevin Janes.
https://doi.org/10.1016/j.bpj.2020.01.045

(16,19–24). Consequently, the repolarization process involves massive rearrangements of the internal, MT-associated structure of the cell. In the third step, the T cell releases at the IS the cytotoxic material (e.g., the pore-forming protein perforin and the apoptosis-inducing granzyme) from vesicles, the lytic granules (25–29), toward the target cell, leading to its destruction (29–39). Although the lytic granule secretion can take place without MTOC repolarization (40) or before it (41), the MTOC-accompanied granule secretion may be required for the killing of resistant cells such as tumor cells.

The IS is partitioned into several supramolecular activation clusters (SMACs) including the distal SMAC, peripheral SMAC (pSMAC), and the central SMAC (cSMAC) (7,9,11,42,43), in which T cell receptors (cSMAC) and adhesion molecules are organized. Moreover, the engagement with the target cell results in the formation of actin and actomyosin networks at the IS (44). Dynein, a minus-end-directed (toward the MTOC) molecular motor protein anchored at the cell cortex, is absolutely necessary for the repolarization to take place, as was experimentally demonstrated with knock-out experiments (45) analogous to dynein exerting forces against anchor proteins fixed at the cell cortex during mitosis (46–49).

Once the T cell is activated, the adaptor protein ADAP forms a ring at the periphery of the IS with which dynein colocalizes (50,51). Concerning the underlying mechanism, it was proposed that the repolarization is driven by the cortical sliding mechanism (50,52), in which dyneins anchored at the cell cortex step on the MT toward the minus end and thus pull the MTOC toward the IS. The first experimental indications for cortical sliding came from observation of cytoskeleton movement using polarization light microscopy (17). Subsequent experiments indicate that the IS periphery, in particular the ring-shaped pSMAC, is the region where dyneins attach to and pull on MTs (17,50).

The repositioning was observed in various experiments. Focused activation of the photoactivable peptide-MHC on the glass surface was used in (53). In (16), the repositioning was observed alongside with the rotation of the mitochondria, which provided evidence that the mitochondria are dragged with the MT cytoskeleton. Detailed observations were made by Yi et al. (14), providing new insight into the mechanism of the repolarization. In (14), an optical trap was used to place a target cell so that the initial point of contact is in diametrical opposition to the current position of the MTOC, which allowed for dynamical imagining in a quantitative fashion. During the experiment, the deformations and changes in MT structures were observed and the position of the MTOC was tracked. First of all, Yi et al. (14) provided strong experimental evidence against the cortical sliding mechanism. Instead, the observations indicate that the MTOC is driven by a capture-shrinkage mechanism (54) localized in a narrow central region of the IS. The capture-shrinkage mechanism involves dynein interacting in an end-on fashion with the plus end of a MT, which is fixed in a position on the membrane of the cell where the MT depolymerizes. The MT shrinkage part happens plausibly because dynein pulls the MT plus end against the cell membrane, which increases the force-dependent MT depolymerization rate (54).

In sequences of microscope pictures, (14) showed that MTs reach from the MTOC to the IS and bend alongside the cell membrane. Subsequently, MTs form a narrow stalk connecting the MTOC with the center of the IS. The plus end of MTs in the stalk, while captured in the center of the IS, straighten (probably under tension due to the dynein pulling at the plus end) and shrink by depolymerization at the capture point. Consequently, the MTOC is dragged toward the center of IS, which invaginates into the cell, further proving the location of the main pulling force. When the MT depolymerization was inhibited by taxol, the MTOC repositioning slowed down substantially. These observations supported the hypothesis that the capture-shrinkage mechanism plays a major role. However, the velocity of the MTOC repositioning is not always an advantage because time is necessarily for the killing of target cells in hostile environments (55) and might be beneficial for slower killing processes (56). Additionally, Yi et al. (14) reported that the repositioning is biphasic and that the two phases differ in the velocity of the MTOC and the orientation of its movement. In the first, so-called polarization phase, the MTOC travels quickly around the nucleus of the cell in a circular manner. The polarization phase ends when the MTOC is approximately 2 μm from the center of the IS. Subsequently, during the second, "docking" phase, the MTOC travels directly toward the IS with a substantially decreased velocity.

The cortical sliding mechanism alone was previously analyzed with a deterministic mechanical model (57), in which it was demonstrated that mechanism is capable of reorienting the MTOC into a position under the IS underneath certain conditions. Furthermore, oscillations between two ISs were studied in different situations. Nevertheless, the forces in the model were deterministic, neglecting the stochastic nature of dynein attachment, detachment, and stepping, leaving various experimental observations unexplained such as, for instance, the preferential attachment of MTs to a dynein anchored in the periphery of the IS.

Sarkar et al. (58) hypothesized that dynamic MTs find the central region of the IS, where they can be captured by a dynein by growing from the MTOC in random directions, analogous to the search and capture mechanism during the formation of the mitotic MT cytoskeleton. Once MTs attach to the dynein in the central region of the IS, the relocation of the MTOC starts, which is the process that is analyzed in this work.

Despite these detailed experimental observations, many aspects of the internal mechanisms driving the relocation of the MTOC during the T cell repolarization remain poorly

understood, like the cause of the transition from the polarization to the docking phase. Yi et al. argue that a resistive force emerges when the MTOC-IS distance is around 2 μm, leading to a reduction in the MTOC's velocity. The potential causes are physical impediments to the MTOC's translation or a reduced attachment or a force development of molecular motors. Moreover, the experiments of Yi et al. were performed with specific initial positions of the IS and the MTOC being diametrically opposed. The question arises whether the observed dominance of the capture-shrinkage mechanism would be robust in other naturally occurring situations in which the initial position of the MTOC is not in diametrical opposition to the IS. If capture-shrinkage is the truly dominant mechanism, what is the role of cortical sliding? Finally, why are cortically sliding MTs caught just on the periphery of the IS (17), and is it caused purely by the colocalization of dyneins with the ADAP ring (50)? The answers to these questions are still elusive, and in this work, we analyze them in the framework of a quantitative theoretical model for the relocation of the MTOC after the IS formation. Although this study focuses on the T cell, NK cells display the same kind of phenomenology: IS formation, MTOC relocation, and the release of lytic granules.

We distribute our analysis into two consecutive publications. In this first publication, we describe the theoretical model we use and present our results focusing on the experiments described in (14,17,50) and on an analysis of the two mechanisms: cortical sliding and capture-shrinkage. This comprises the setup in which the T cell has one IS and the initial positions of the IS and the MTOC are diametrically opposed to each other.

A subsequent, second, publication will focus on quantitative predictions of our model for situations that have not yet been analyzed experimentally. There, we will focus on the repolarization after initial configurations not realized in (43), which will also provide additional insight into the different effects of the two mechanisms, cortical sliding and capture-shrinkage. Moreover, we will analyze the eventually oscillating MT/MTOC movement with two ISs.

METHODS

Computational model

The cell and its nucleus are modeled as two concentric spheres of the radius 5 and 3.8 μm, respectively. The model of the cytoskeleton consists of MTs and the MTOC; see Fig. 1. MTs are thin filaments with a diameter of ~25 nm (59–61). The measured values of the flexural rigidity vary between experiments (62,63); in our model, we take 2.2×10^{-23} nm^2 (64), yielding a persistence length larger than 5 mm that exceeds the size of the cell by three orders of magnitude. A single MT is represented by a bead-rod model (65). Because repolarization occurs on a timescale of seconds, the growth of MTs is neglected. The beads move under the influence of forces to be described below (and defined in detail in the Supporting Materials and Methods: bending, drag, molecular motor, and stochastic forces). Assuming zero longitudinal elasticity of the MTs, we use constrained Langevin dynamics to model the motion of the MTs; see the Supporting Materials and Methods. Repulsive forces acting on the MT segments confine the cytoskeleton between the nucleus and the cell membrane.

The MTOC is a large protein complex that has a complex structure composed of mother and daughter centrioles (66–69) embedded in the pericentriolar material (70–72). MTs nucleate from γ-tubulin-containing ring structures within the pericentriolar material mainly at the appendages of the mother centriole (66,73). MTs can sprout from the MTOC in all directions. MTs whose original direction is approximately parallel to the membrane of the cell will continue to grow to the cell periphery. Other MTs will soon hit the wall of the cell or its nucleus. Such MTs can either bend and assume a new direction parallel to the cell membrane or undergo the MT catastrophe. Therefore, long MTs are seemingly always sprouting from the MTOC in one plane, as can be seen in (14). Consequently, we model the MTOC as a planar, rigid polygon structure (Fig. S3) from which MTs emanate in random directions by fixing the positions and directions of their first segment (Fig. S4). MTs sprout from the MTOC to the cell periphery; see Fig. 1 *a*.

Unattached dynein is represented just with one point on the surface of the cell. If the dynein is closer to the MT than L_0, protein attaches with a probability p_a. Dynein motors are distributed randomly in specific, spatially varying concentrations on the cell boundary. Attached dynein is represented by a fixed anchor point located on the cell boundary and an attachment point located on an MT, both being connected by an elastic stalk of a length L_0 (74,75). The force exerted on an MT F_i^{Dynein} depends on the stalk's

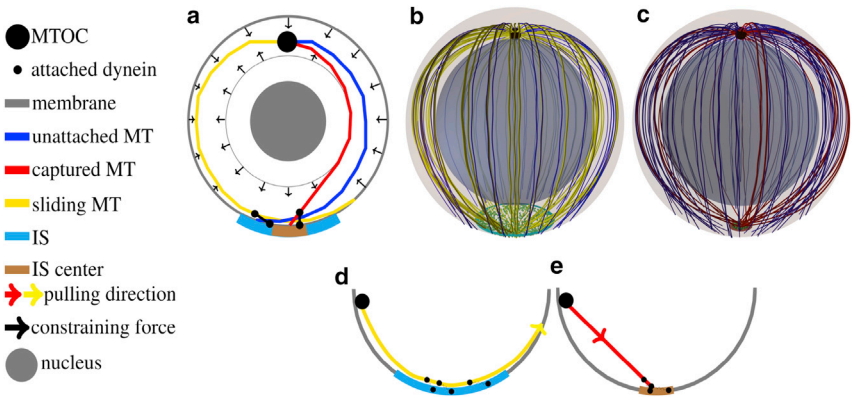

FIGURE 1 (*a–c*) Sketch of the model. (*a*) A two-dimensional cross-section of the model is shown. MTs sprout from the MTOC, and their movement is confined by constraining forces from the cell membrane and the nucleus. MTs are attached to dynein motors in the IS, and they are pulled by the capture-shrinkage or the cortical sliding mechanism. (*b* and *c*) A three-dimensional sketch of the cell model is given. The outer transparent and inner spheres represent the cell membrane and the nucleus of the cell, respectively. (*b*) The blue disk represents the IS, where cortical sliding dynein is anchored. Small green dots in the IS represent randomly distributed dynein. (*c*) The brown disk represents the central region of the IS where the capture-shrinkage dynein is anchored. (*d* and *e*) A sketch of the cortical sliding mechanism (*d*) and the capture-shrinkage mechanism (*e*) is shown. Small black dots on the membrane: dynein anchor points, small black dots on the MTs: attachment points. Note that MTs depolymerize when pulled by capture-shrinkage dynein toward the membrane. To see this figure in color, go online.

elastic modulus k_{Dynein} and its prolongation. The dynein stepping depends on the magnitude of the force and its orientation. If the force is parallel to the preferred direction of the stepping, the attachment point moves one step to the MT minus end (toward the MTOC) with a constant probability p_{-}. If the orientation of the force is opposite and its magnitude smaller than a stall force F_S, dynein makes one step toward the minus end with a force-dependent probability. If $|F_i^{\mathrm{Dynein}}| > F_S$ and the force has a unfavorable direction, the dynein makes one step to the plus end with a constant probability p_{+}. The steps of the dynein have varying lengths (75), but for simplicity, we set it to the most frequently measured value of $d_{\mathrm{step}} = 8$ nm. The probability of detachment, p_{detach}, increases with the force.

Experimentally, two mechanisms by which the dynein act on MTs have been identified: cortical sliding (17), in which MTs under the effect of dynein move tangentially along the membrane, and capture-shrinkage (14), by which MTs under the effect of dynein are reeled in toward the membrane and concomitantly depolymerized (sketched in Fig. 1, *d* and *e*).

The IS is divided into two regions: the center, where dyneins act on MTs via the capture-shrinkage mechanism (14), and the complete IS, where dyneins act via the cortical sliding mechanism. Each region is modeled as an intersection of the cell sphere with a cylinder, 1, with radius $R_{\mathrm{IS}} = 2\ \mu$m for the complete IS and $R_{\mathrm{CIS}} = 0.4\ \mu$m for the central region. Dyneins are distributed randomly with uniform area density ρ_{IS} in the small central region, denoted as capture-shrinkage dynein, and density $\tilde{\rho}_{\mathrm{IS}}$ in the larger region of the whole IS, denoted as cortical sliding dynein.

RESULTS

We analyzed the role of the cortical sliding and capture-shrinkage mechanisms and their combined effect during the repolarization by computer simulations of the model defined in the previous section. The density of dyneins anchored at the IS, $\tilde{\rho}_{IS}$, and the central region of the IS, ρ_{IS}, are unknown model parameters, which we therefore vary over a broad range between 0 (no anchored dynein) and 1000 $\mu\mathrm{m}^{-2}$ (the maximal number of anchored dynein because of the lateral size of dyneins; see Supporting Materials and Methods, Section S1.1.5). During the integration of the equation of motion, various quantities are calculated: the distance between the center of the MTOC and the IS, d_{MIS}; the number of dyneins attached to the MTs, N_{dm}; the velocity of the MTOC, v_{MTOC}; and the distance between the MTOC and the center of the cell, d_{MC}. For each point in the parameter space, these quantities were averaged over 500 simulation runs. Each simulation run is initialized with the mechanical equilibrium (minimal elastic energy) configuration of the MT/MTOC-system and all dyneins being detached. Results are shown with the standard deviation as error bars only when they are larger than the symbol size.

Capture-shrinkage mechanism

The repositioning process under the effect of the capture-shrinkage mechanism is visualized in Fig. 2. In Fig. 2, *a* and *d*, it can be seen that initially, the attached MTs aim from the MTOC in all directions. Subsequently, the stalk of MTs is almost formed in the middle phase of the repositioning (Fig. 2, *b* and *e*), and it is fully formed as the MTOC approaches the IS; see Fig. 2, *c* and *f* and Video S1 showing the time evolution of the MT cytoskeleton configuration under the effect of the capture-shrinkage mechanism with 100 MTs and the dynein density $\rho_{\mathrm{IS}} = 100\ \mu\mathrm{m}^{-2}$.

The process can be divided into three phases based on the time evolution of the MTOC velocity; see Fig. 3 *b*. In the first phase, when the distance between the MTOC and the center of the IS is $\overline{d}_{\mathrm{MIS}} > 8.8\ \mu$m, the velocity changes rapidly in the first seconds of the process and then falls to a local minimum. In the second phase, the velocity continually increases to a maximum, and then in the third phase, it decreases again. By comparison of Fig. 3, *b* and *c*, it can be seen that the time evolution of the velocity corresponds to the time evolution of the number of dyneins acting on MTs. The evolution of the number of attached dyneins

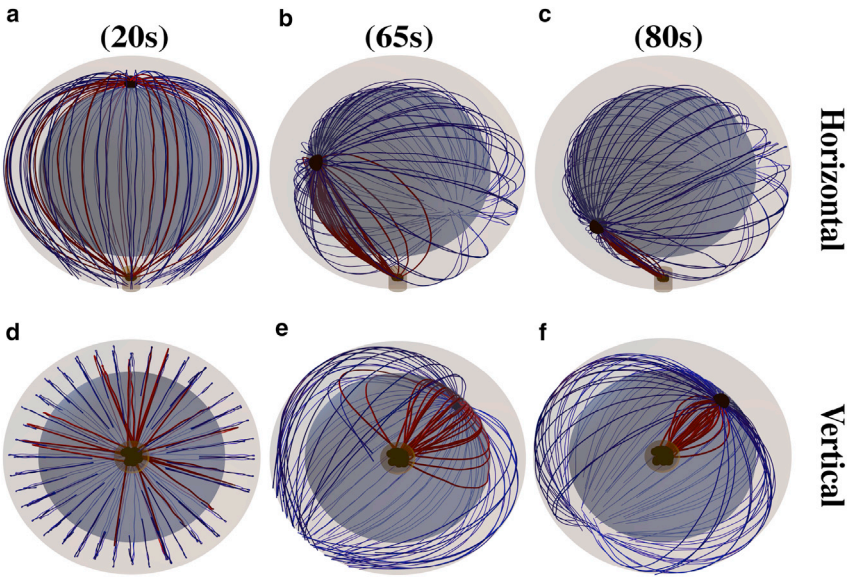

FIGURE 2 Snapshots from the time evolution of the MT cytoskeleton configuration under the effect of the capture-shrinkage mechanism alone (dynein density $\rho_{\mathrm{IS}} = 100\ \mu\mathrm{m}^{-2}$). MTs are connected to the MTOC indicated by the large black sphere. Blue and red curves are unattached and attached MTs. Small black spheres in the IS represent dyneins. The brown cylinder indicates the center of the IS, where the capture-shrinkage dyneins are located. (*a* and *d*) $d_{\mathrm{MIS}} = 9\ \mu$m. Initially, the attached MTs sprout from the MTOC in all directions. (*b* and *e*) $d_{\mathrm{MIS}} = 6\ \mu$m. As time progresses, MTs form a stalk connecting the MTOC and the IS. (*c* and *f*) $d_{\mathrm{MIS}} = 2.5\ \mu$m. The stalk is fully formed, and it shortens as the MTOC approaches the IS. To see this figure in color, go online.

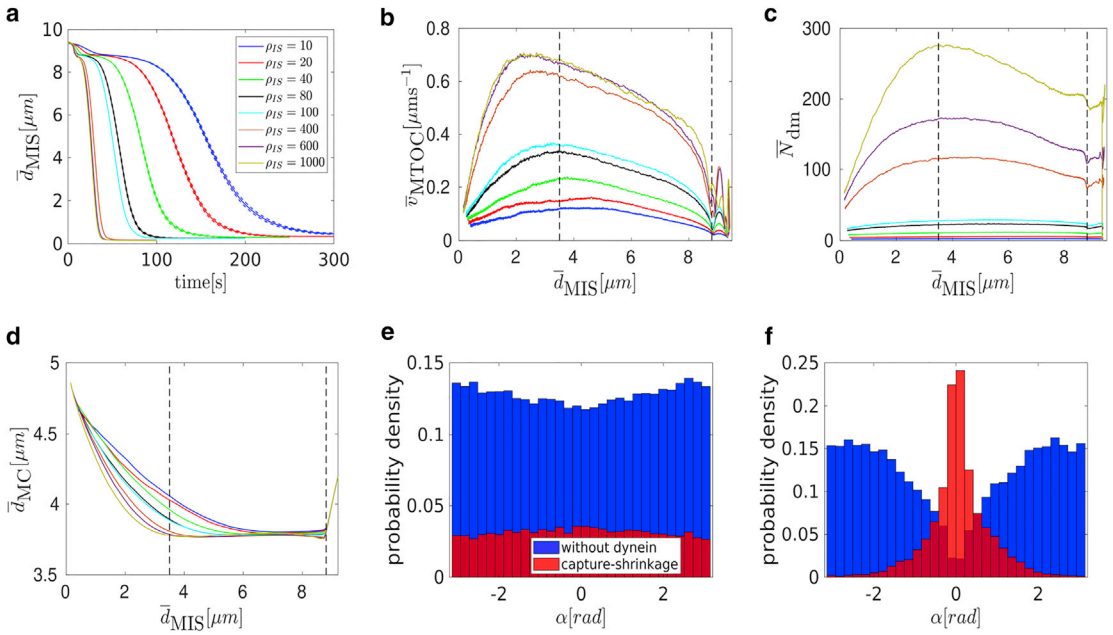

FIGURE 3 Capture-shrinkage mechanism: (*a*) the dependence of the average MTOC-IS distance $\overline{d}_{MIS}$ on time. The error bars are represented by dashed lines and are plotted only if bigger than a symbol size. (*b–d*) Dependencies of the average MTOC velocity $\overline{v}_{MTOC}$ (*b*), the number of dyneins acting on microtubules $\overline{N}_{dm}$ (*c*), and the MTOC-center distance $\overline{d}_{MC}$ (*d*) on the average MTOC-IS distance are shown. Black dashed lines denote transitions between different phases of the repositioning process. (*e* and *f*) Probability distributions of the angles between the first MT segments and the direction of the MTOC movement for a dynein density $\rho_{IS} = 100\ \mu m^{-2}$ (*e*), $t = 1$ s, $\overline{d}_{MIS} \sim 9\ \mu m$ are given. (*f*) $t = 60$ s, $\overline{d}_{MIS} \sim 5\ \mu m$. To see this figure in color, go online.

during the first phase can be understood from an analysis of Figs. 2, *a* and *b* and 3 *d*. At the beginning of the simulations, a substantial number of MTs intersects the IS (visually demonstrated in Fig. 2, *a* and *d*), resulting in a fast increase of the number of attached dyneins. Because the MTs attached to dynein sprout from the MTOC in every direction (cf. Fig. 3 *e*), the MTOC moves toward the IS and, simultaneously, to the nucleus of the cell (see Fig. 3 *d*). As the MTOC approaches the nucleus of the cell, the nucleus starts to oppose the movement by repelling the MTs and, at the end of the first phase, the MTOC. Therefore, as the pulling force of the dyneins is opposed by the nucleus, the dyneins detach because the detachment rate is force dependent.

The increase of the number of attached dyneins $\overline{N}_{dm}$ in the second phase can be explained by considering the fact that the MTOC slides over the surface of the nucleus and the MT stalk forms. At the beginning, the nucleus presents an obstacle between the MTOC and the IS; see Fig. 2 *a*. The opposing force from the nucleus decreases with the approach of the MTOC toward the IS. At the end of the repositioning, the nucleus no longer stands between the two objects; see Fig. 2, *c* and *f*. Therefore, the opposing force from the nucleus contributing to dynein detachment decreases. More importantly, attached MTs form the MT stalk. The angle α between the first segment of the MT and the direction of the MTOC movement is used to describe the deformation of the cytoskeleton structure and the stalk formation. At the beginning of the simulation (the first phase and the beginning of the second), attached MTs aim in every direction (see Fig. 3 *e*, visualized in Fig. 2, *a* and *d*). Therefore, the dyneins pull in multiple directions, which makes them oppose each other, leading to dynein detachment. After a few seconds, the MTOC travels in the direction of the biggest pulling force. Consequently, the attached MTs form a stalk as the simulation progresses, and dyneins act in alignment; see Figs. 2, *b* and *e* and 3 *f*. They no longer oppose each other but share the load from opposing forces. Consequently, the detachment probability of dynein decreases with the opposing force, and the number of attached dyneins increases.

The number of dyneins decreases in the final phase when $\overline{d}_{MIS} < 3.5\ \mu m$; see Fig. 3 *c*. Unattached MTs in the IS are pushed backward by viscous drag as the MTOC moves to the IS. As a result, one observes an "opening" of the MT cytoskeleton; cf. Figs. 2, *c* and *f* and 3 *e*. Unattached MTs do not intersect the IS (see Fig. 3 *f*) and cannot attach to dyneins. The attached MTs shorten because of the depolymerization, further lowering the probability of dynein attachment. Moreover, an opposing force arises from the cytoskeleton being dragged from the nucleus to the membrane (see Fig. 3 *d*), causing the detachment of dyneins because the detachment rate is force dependent.

To summarize, the trajectory of the MTOC toward the IS displays three phases, in which the two longer phases have also been reported in experiment (14), but not the short initial phase. First, the MTOC descends to the nucleus (see Fig. 3, *a* and *d*); then it moves to the IS quickly and slows down during the last 2 μm (see Fig. 3 *b*). Once the MTOC bypasses the nucleus, it moves away, switching

from a purely circular to partially radial movement (see Fig. 3 *d*). The variation of the MTOC velocity, its modulus, and its direction are clearly visible in Video S2, showing a simulation with a smaller nucleus radius $r_N = 3.3$ μm. Note that the duration of the complete repositioning process in the experiments is ~60–90 s, which our model predicts to be achieved by a dynein density of 80–200 μm^{-2}.

Cortical sliding mechanism

For low, medium, and high densities, one observes for each a different characteristic behavior. In the regime of low dynein densities ($\tilde{\rho}_{IS} < 100$ μm^{-2}), the repolarization velocity increases with the dynein density, and the MTOC moves directly to the IS; see Fig. 5 *a*. For medium dynein densities (100 $\mu m^{-2} \leq \tilde{\rho}_{IS} < 500$ μm^{-2}), the MTOC movement is more complex; see Fig. 7 *a*. For high dynein densities ($\tilde{\rho}_{IS} > 500$ μm^{-2}), the repolarization velocity surprisingly decreases with $\tilde{\rho}_{IS}$; see Fig. 8 *a*.

Cortical sliding with low dynein densities

Video S3 shows MTOC repositioning under the effect of the cortical sliding mechanism with $\tilde{\rho}_{IS} = 60$ μm^{-2}. It shows MTs sprouting in all directions in the initial stage, the subsequent stalk formation, and the final slowing down of the MTOC. In Fig. 5 *b*, the dependence of the MTOC velocity on the MTOC-IS distance is shown. As in the case of the capture-shrinkage mechanism, the time evolution of the MTOC velocity can be divided into three phases. However, the transition points between the second and the third phase depend on the density $\tilde{\rho}_{IS}$. Similarly to the case of the capture-shrinkage mechanism, the behavior in the first phase can be explained by the interplay of fast-attaching dyneins and forces from the nucleus. In the second phase, the velocity of the MTOC increases despite a continuously decreasing number of attached dyneins (see Fig. 5, *b* and *c*), which is due to the alignment of the MTs. Initially, attached MTs aim in all directions (see Fig. 5 *e*), as for the capture-shrinkage mechanism (cf. Fig. 4, *a* and *d*). Consequently, MTs whose original orientation does not correspond to the movement of the MTOC detach from dynein (see Figs. 4, *b* and *e* and 5 *f*). The probability density in the intermediate state of the repositioning ($\overline{d}_{MIS} \sim 5$ μm) shows that attached MTs are aligned and less in numbers. The MTOC does not significantly recede from the nucleus at the end of the repositioning (see Fig. 5 *d*), which implies that the MTs do not follow the cell membrane (with the capture-shrinkage mechanism, MTs always touch the membrane); see Fig. 4, *c* and *f*. Consequently, the attachment probability is lower and leads to the decrease in velocity in the third phase.

Cortical sliding with medium dynein densities

The differences between the behavior with low and medium dynein densities for the cortical sliding mechanism are analyzed in this section. Video S4 shows the repositioning with $\tilde{\rho}_{IS} = 200$ μm^{-2}. The repositioning is very fast, and the MT cytoskeleton is considerably deformed. Moreover, the MTOC passes the IS and subsequently returns to the center of IS. 5 s after the initialization, MTs in all directions are attached (see Fig. 6, *a* and *d*), but the direction of the MTOC motion is already established (see Fig. 7 *b*). Contrary to the case of low densities, the dynein forces are sufficiently strong to hold attached MTs. Subsequently, some MTs do not detach but take a direction partially aligned to the MTOC movement (see Fig. 7, *c* and *d*). Moreover, almost all MTs aligned with the MTOC motion are attached to dyneins (compare Figs. 5 *f* and 7 *d*). Consequently, the large majority of MTs are aligned with the direction of movement of the MTOC movement, causing a substantial increase of the MTOC velocity. By comparing the temporal evolution of the MTOC-IS distance $\overline{d}_{IS(t)}$ for small, medium, and large

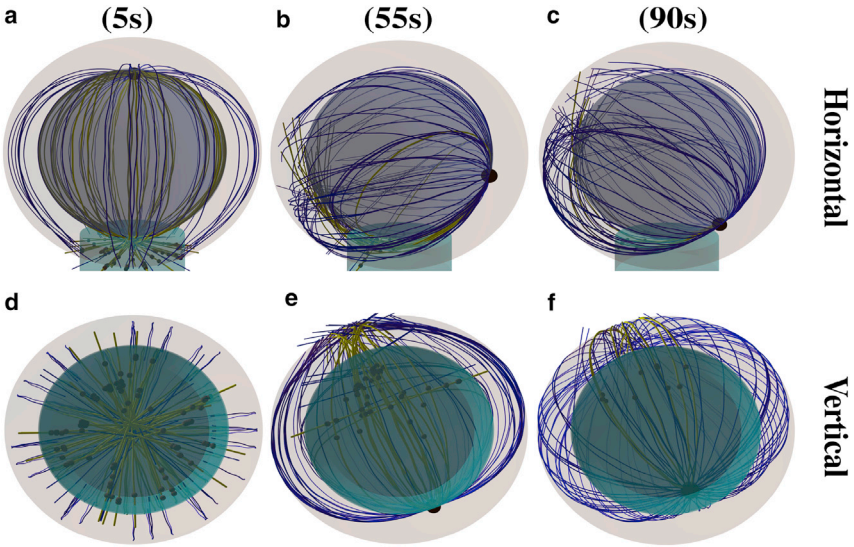

FIGURE 4 Snapshots from the time evolution of the MT cytoskeleton configuration under the effect of cortical sliding mechanism with a low dynein density, $\tilde{\rho}_{IS} = 60$ μm^{-2}. The cyan cylinder indicates the IS area. Blue and yellow lines are unattached and attached MTs, respectively. The black spheres in the IS are the positions of dyneins attached to MTs. (*a* and *d*) $\overline{d}_{MIS} = 9$ μm. Originally, the attached MTs aim from the MTOC in every direction. (*b* and *e*) $\overline{d}_{MIS} = 4.5$ μm. MTs attached to dynein aim predominantly in one direction. (*c* and *f*) $\overline{d}_{MIS} = 1.5$ μm. Just a few MTs remain under the actions of cortical sliding, and they rarely touch the surface of the cell in the IS. To see this figure in color, go online.

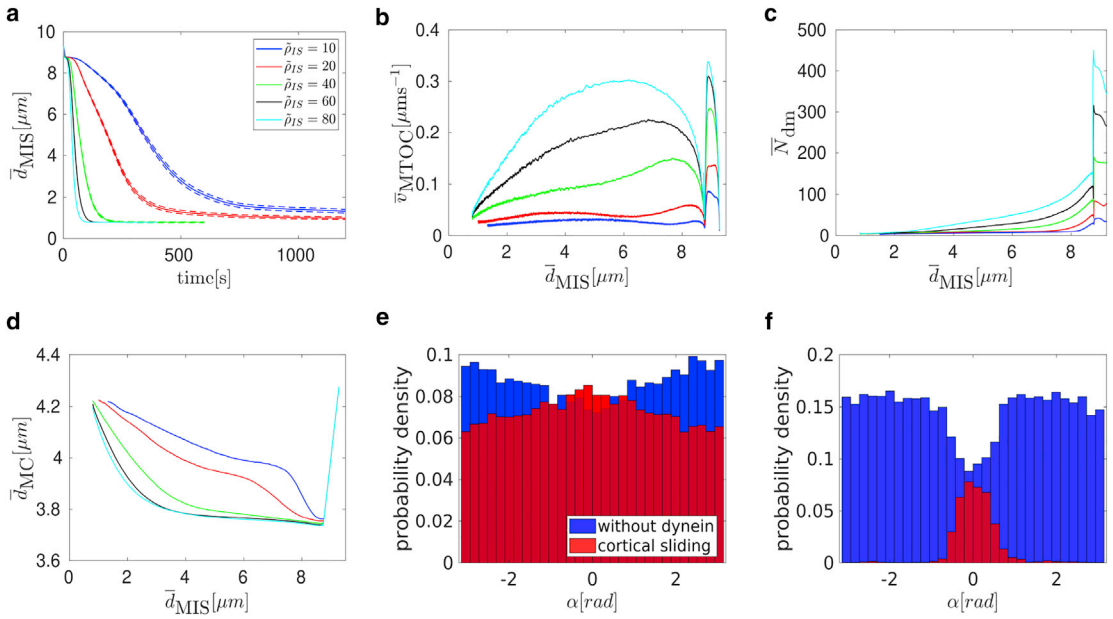

FIGURE 5 Cortical sliding with low dynein densities $\tilde{\rho}_{IS}$. (*a*) The dependence of the average MTOC-IS distance $\overline{d}_{MIS}$ on time is shown. The error bars are represented by dashed lines and are plotted only if bigger than a symbol size. (*b–d*) Dependencies of the average MTOC velocity $\overline{v}_{MTOC}$ (*b*), number of dyneins acting on MTs $\overline{N}_{dm}$ (*c*), and the MTOC-center distance $\overline{d}_{MC}$ (*d*) on the average MTOC-IS distance are shown. (*e* and *f*) Probability distributions of the angles α between the first MT segment and the MTOC motion, $\tilde{\rho}_{IS} = 60\ \mu m^{-2}$, are shown. (*e*) $t = 5$ s, $\overline{d}_{MIS} \sim 9\ \mu m$. (*f*) $t = 65$ s, $\overline{d}_{MIS} \sim 5\ \mu m$. To see this figure in color, go online.

dynein densities (Figs. 5 *a*, 7 *a*, and 8 *a*), one observes that the velocity of the MTOC is maximal for medium densities of cortical sliding dyneins (see also Fig. 9, *a* and *b* below). Moreover, by comparing the configuration snapshots for low and high densities (Fig. 4, *b* and *e* and 6, *b* and *e*), one observes that the strong forces exerted at high dynein densities cause large deformations of the MT cytoskeleton.

Because of the deformation of the cytoskeleton, a large number of MTs are attached to dynein at the end of the repositioning (see Fig. 7 *d*), and dyneins are predominantly found at the opposite side of the IS (compared to the MTOC). Because of the attachment, the MTOC passes the center of the IS (see Fig. 7 *a*) and the anchor points of certain dynein motors (see Fig. 6, *c* and *f*). The MTs are attached to anchor points, so the probability density of α changes, and the majority of MTs are behind the MTOC (see Fig. 7 *e*). When the MTOC returns to the IS, the probability density levels (see Fig. 7 *f*), and dynein detaches.

Cortical sliding with high dynein densities

An example for repositioning under the effect of cortical sliding with a high dynein density $\tilde{\rho}_{IS} = 1000\ \mu m^{-2}$ is shown in Video S5. As the area density $\tilde{\rho}_{IS}$ rises, the MTs are more and more attached at the periphery (see Fig. 8 *d*). This is further demonstrated by Fig. 8, *e* and *f* (the center of the IS is almost depopulated when $\tilde{\rho}_{IS} = 1000\ \mu m^{-2}$). The reason is that there are a sufficient number of dyneins to firmly catch the MTs passing just the periphery of the IS. The higher number of MTs also logically means bigger pulling forces on MTs. In a spherical cell, dyneins act in competition, which leads to dynein detachment. The bigger the competition is, the more frequent the detachment, as can be seen in Fig. 8 *b*, in which the highest number of attached dyneins corresponds to the lowest area density.

Constantly attaching and detaching dyneins does not allow MTs to align with the direction of the MTOC movement. Subsequently, the MTOC "lingers" behind the nucleus before it moves to the IS as the dominant orientation of attached MTs forms slowly. The duration of this inactivity rises with $\tilde{\rho}_{IS}$ (see Fig. 8 *a*). Even when the dominant direction is established, MTs are still attached in every direction, slowing down the movement (see Fig. 8 *c*). Therefore, the slowing in the third section (cf. Fig. 8 *a*) is caused by two effects: first, the misalignment of MTs, resulting in contradictory pulling forces and a lower number of attached dyneins; second, the increasing probability of attachment at the periphery, resulting in MTs being pulled to different places and increasingly contradicting each other as the MTOC approaches the IS.

Comparison of cortical sliding and capture-shrinkage

In this section, two mechanisms are compared in terms of MTOC velocity: times and final MTOC-IS distances. The biological motivation is that the velocity (times) indicates the efficiency of transmission of the force of dynein on the cytoskeleton, and the final distance determines the

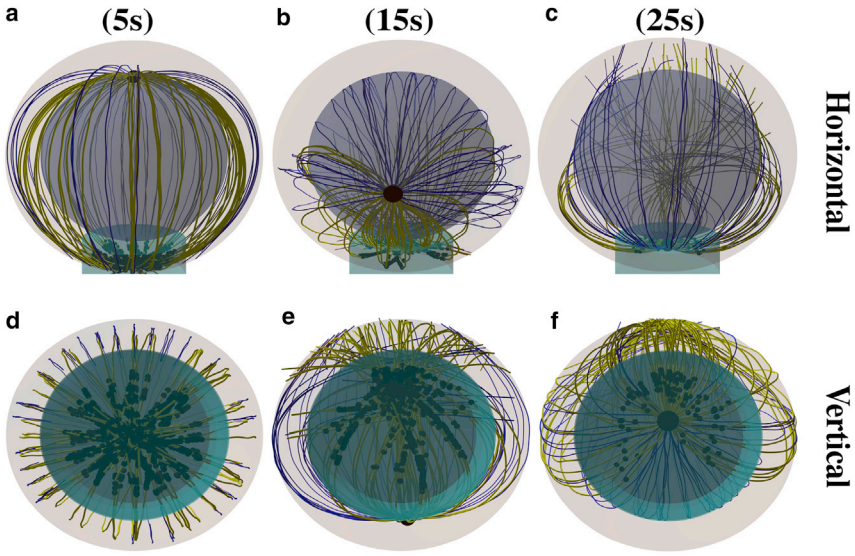

FIGURE 6 Snapshots from the time evolution of the MT cytoskeleton configuration under the effect of cortical sliding alone, with a medium area density of the dynein $\tilde{\rho}_{IS} = 200\ \mu m^{-2}$) from two perspectives. (*a* and *c*) $\overline{d}_{MIS} = 9\ \mu m$. MTs sprout from the MTOC in all directions. (*b* and *d*) $\overline{d}_{MIS} = 5\ \mu m$. The majority of MTs are attached, and the MT cytoskeleton is deformed. (*c* and *e*) $\overline{d}_{MIS} = 1\ \mu m$. At the end of the repositioning, the MTOC passed the center of the IS, and attached MTs aim in all directions. To see this figure in color, go online.

completion of the repositioning. In the previous sections, the repositioning was divided into three phases based on the MTOC velocity (see Figs. 3 and 5), which enabled the analysis of the dynamics based on the attached dyneins and deformations of the cytoskeleton structure.

To analyze average velocity, the repositioning is divided into three phases based on the MTOC-IS distance: the activation, the first, and the second phase. This approach will later enable a comparison with experimental results. The activation phase ends when $d_{MIS} \leq 8.2\ \mu m$ (identical with the first phase based on the MTOC velocity). Although the activation phase is important for the observation of the influence of dynein motors (see Figs. 3 *c*, 5 *c*, and 8 *b*), the phase lacks experimental analogy because in reality, the IS, along with a high dynein area density, is not created instantly. Therefore, it will not be further analyzed. In the first phase, the MTOC-IS distance $8.2\ \mu m > d_{MIS} > d_f + 1\ \mu m$, where d_f is the final MTOC-IS distance, which depends on the area density and mechanism. The second phase comprises the last micrometer of the MTOC journey.

The MTOC velocity in the capture-shrinkage repositioning increases with the area density of dyneins for both phases (see Fig. 9 *a*). The development of the average MTOC velocity of the cortical sliding repolarization is more difficult because it rises to its maximum (middle densities) (see Fig. 9 *a*) and then falls sharply. The velocity of the cortical sliding repositionings is lower except when considering middle area densities of the cortical sliding dynein. Moreover, for the low and high densities, the velocity of capture-shrinkage is more than two times the velocity of cortical sliding (see Fig. 9 *a*). The times of repositioning evolve accordingly (see Fig. 9 *c*). Times are longer for the case of capture-shrinkage only when ρ corresponds to the middle densities of cortical sliding (see Fig. 9 *a*).

The final MTOC-IS distance decreases with the rising ρ in the case of sole capture-shrinkage (see Fig. 9 *b*). In the case of cortical sliding, the situation is more complicated because of the lack of an anchor point. The large final distances at low area densities are caused by the insufficient pulling force. The shortest distance is at the end of low area densities $\rho = 80\ \mu m^{-2}$, which is caused by the fact that the formation of the narrow MT stalk, in which MTs pull in alignment, is limited just to low densities (see Figs. 5 *e*, 7 *c*, and 8 *c*). Then, we can observe a steady rise in final distances caused by the growing attachment of MTs at the peripheries as $\tilde{\rho}_{IS}$ causes the increasing competition of pulling forces in the final stages of the polarization.

Fig. 9 *c* explains the lower MTOC velocity for cortical sliding. First of all, let us notice that the three regimes of the cortical sliding behavior are visible in Fig. 9 *c*. We can see that the increasing $\tilde{\rho}_{IS}$ causes MT attachment on the periphery of the IS, as was already suggested by Fig. 8, *d–f*. Moreover, the attached dynein is always predominantly at the periphery because the average distance for the uniform distribution of dynein is $\overline{r}_{IS} = (1/2)R_{IS} = 1\ \mu m$. Therefore, as the MTOC approaches the IS, MTs are pulled to different locations, and the forces of dynein oppose each other and cause the dynein detachment.

The capture-shrinkage mechanism is faster, with the relatively narrow exception of the middle area densities. Cortical sliding never achieves shorter distances in comparison to capture-shrinkage; moreover, in the case of high or low densities, the final distances differ substantially. Fig. 9 shows the dependencies on area density. Nevertheless, in the case of capture-shrinkage, we consider just the density in the center of the IS. We should remind the reader that the radii of the center and the entire IS are $R_{CIS} = 0.4\ \mu m$ and $R_{IS} = 2\ \mu m$. Because the number of dyneins depends on the area, the number of dyneins in the IS $N_{IS} = 25 \times N_{CIS}$, where N_{CIS} is the number of dyneins in the center of the IS. Consequently, Fig. 9 confirms that the capture-shrinkage mechanism is the main driving force of the repositioning because

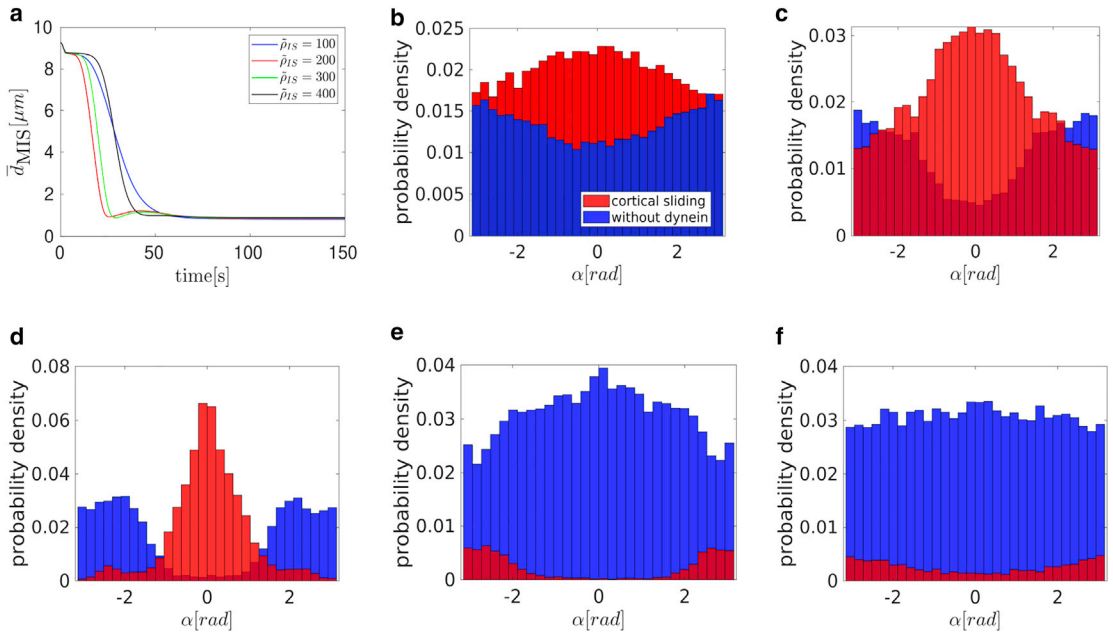

FIGURE 7 Cortical sliding mechanism with medium dynein densities $\tilde{\rho}_{\mathrm{IS}}$. (*a*) The dependence of the MTOC-IS distance $\overline{d}_{\mathrm{MIS}}$ on time is shown. Probability distributions of the angles α between the first MT segment and the MTOC motion, $\tilde{\rho}_{\mathrm{IS}} = 200\ \mu\mathrm{m}^{-2}$, are shown. (*b*) $t = 5$ s, $\overline{d}_{\mathrm{MIS}} \sim 9\ \mu$m. (*c*) $t = 15$ s, $\overline{d}_{\mathrm{MIS}} \sim 6\ \mu$m. (*d*) $t = 20$ s, $\overline{d}_{\mathrm{MIS}} \sim 2.5\ \mu$m. (*e*) $t = 25$ s, $\overline{d}_{\mathrm{MIS}} \sim 1.5\ \mu$m, other side of IS. (*f*) $t = 60$ s, $\overline{d}_{\mathrm{MIS}} \sim 0.8\ \mu$m. To see this figure in color, go online.

this mechanism produces bigger or comparable velocities with just 4% of the dynein motors of cortical sliding. Moreover, the MTOC comes closer to the IS, meaning that the capture-shrinkage mechanism is more likely to finish repositioning. To summarize, considering the lower number of dyneins, the capture-shrinkage mechanism is largely superior in the considered setup. The most important difference between the two mechanisms is the firm, narrow anchor point in case of the capture-shrinkage mechanism. It assures a firm attachment of the MTs (see Fig. 3 *f*) and a geometrical alignment of the pulling forces in all stages of repositioning. The capture-shrinkage mechanism was identified as the main driving force of the repositioning (14), and our model fully supports this statement. In the next section, we will scrutinize the role of cortical sliding.

Combination of capture-shrinkage and cortical sliding

In this section, the interplay between the two mechanisms is analyzed. A comparison of Video S6 (capture-shrinkage, with $\rho_{\mathrm{IS}} = 60\ \mu\mathrm{m}^{-2}$, $\tilde{\rho}_{\mathrm{IS}} = 0\ \mu\mathrm{m}^{-2}$) and Video S7 (both mechanisms combined, $\tilde{\rho}_{\mathrm{IS}} = \rho_{\mathrm{IS}} = 60\ \mu\mathrm{m}^{-2}$) demonstrates the difference between the MT cytoskeleton dynamics under the effect of capture-shrinkage alone and under the effect of both mechanisms combined. The videos show the first few seconds of the process. In the case of sole capture-shrinkage, only long enough MTs attach to the center of the IS. One clearly sees in Video S7 that MTs intersecting the IS and attached to cortical sliding dynein are passed to the center of the IS, where they are captured by cortical sliding dynein. Video S8 shows the complete repositioning of the MTOC under the effect of both mechanisms combined ($\tilde{\rho}_{\mathrm{IS}} = \rho_{\mathrm{IS}} = 60\ \mu\mathrm{m}^{-2}$).

A quantitative analysis in Fig. 10, *a* and *b* shows that the repolarization velocity increases with the cortical sliding density $\tilde{\rho}_{\mathrm{IS}}$ as expected. Quite unexpectedly, it turns out that the average number of attached capture-shrinkage dyneins depends on the density of cortical sliding dyneins $\tilde{\rho}_{\mathrm{IS}}$ and increases with it, as demonstrated by Fig. 10 *c*.

This finding indicates a synergy of the two mechanisms, capture-shrinkage and cortical sliding, and can be explained by the alignment of the MTs during repositioning. The MTs attached to the cortical sliding dyneins tend to align with the MTOC movement, as demonstrated by Fig. 10 *e*, in which the dominant central peak in direction $\alpha = 0$ is caused by capture-shrinkage dyneins, and cortical sliding dyneins provide only two small peaks from angles toward the periphery of the IS. As MTs align with the MTOC movement, they are captured by the capture-shrinkage dyneins in the central region of the IS, and the number of cortical sliding dyneins drops dramatically, as shown in Fig. 10 *d*.

A comparison of the probability densities shown in Fig. 3 *f* for capture-shrinkage alone and Fig. 5 *f* for cortical sliding alone reveals the mechanism by which cortical sliding supports capture-shrinkage. Fig. 3 *f* shows that the unattached MTs are pushed back by friction forces, which leads to the opening of the MT cytoskeleton such that MTs cannot intersect the narrow center of the IS anymore (visualized in Fig. 2 *f*). Attached MTs align with the MTOC movement in the case of cortical sliding (cf. Fig. 5 *f*). Therefore, when both mechanisms are combined, MTs attached by the

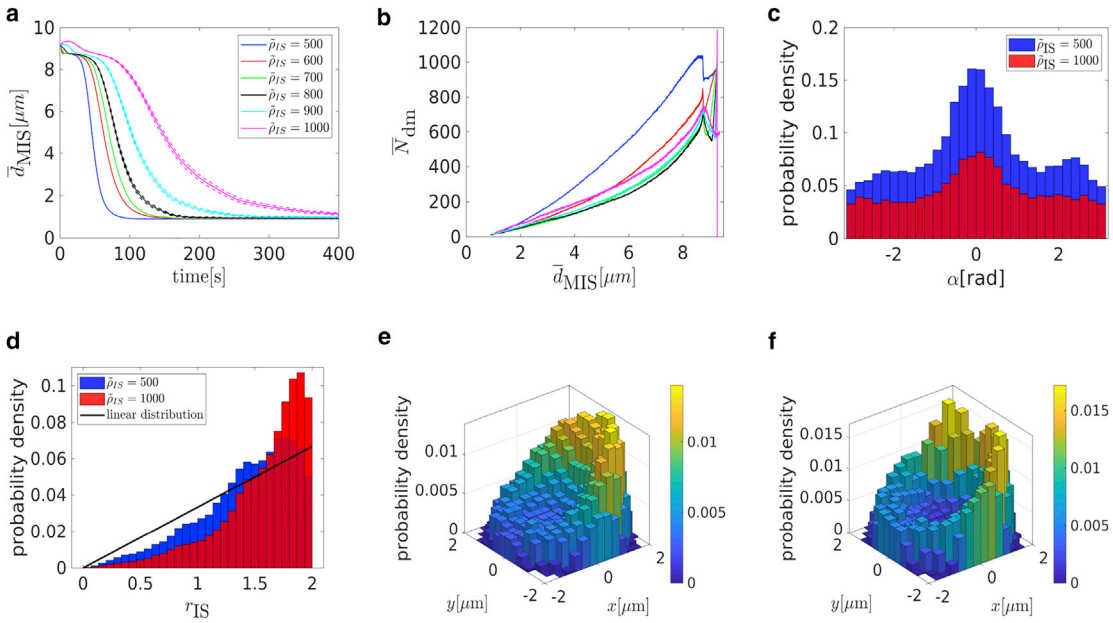

FIGURE 8 Cortical sliding with high dynein densities $\tilde{\rho}_{IS}$. (*a*) The dependence of the average MTOC-IS distance $\overline{d}_{MIS}$ on time is shown. The error bars are represented by dashed lines and are plotted only if bigger than a symbol size. (*b*) The dependence of the average number of dyneins $\overline{N}_{dm}$ on the MTOC-IS distance is shown. (*c*) Probability distribution of the angle α between the first MT segment of attached MTs and the direction of the MTOC motion, $\overline{d}_{MIS} \sim 5$ μm, is shown. (*d*) The probability distribution of the distance of attached dynein anchor points from the axis of the IS r_{IS} when $\overline{d}_{MIS} \sim 5$ μm is shown. (*e* and *f*) The two-dimensional probability density of attached dyneins in the IS, $\overline{d}_{MIS} = 5$ μm, is shown. (*e*) Area density of cortical sliding dyneins $\tilde{\rho}_{IS} = 500$ μm^{-2}. (*f*) $\tilde{\rho}_{IS} = 1000$ μm^{-2}. To see this figure in color, go online.

cortical sliding dyneins are not pushed back by friction, they align with the MTOC movement, and the attachment probability of the capture-shrinkage dynein increases. Comparing the probability density of the angle α for cortical sliding alone (Fig. 5 *f*) with the one for the combined mechanisms (Fig. 10 *e*) demonstrates impressively that most MTs attached to cortical sliding dyneins have detached and attached to capture-shrinkage dyneins.

These observations suggest an answer to the question about the role of the cortical sliding: it passes the MTs to the more efficient capture-shrinkage mechanism. Additionally, it provides a bigger pulling force than for cortical sliding alone because of the fact that the capture-shrinkage mechanism also supports cortical sliding. By comparison of Figs. 5 *c* and 8 *b* with Fig. 10 *d*, one realizes that the dependencies of the number of cortical sliding dyneins on the MTOC-IS distance are very different. As the MTOC approaches the IS, the number of dyneins acting on MTs decreases in the case of sole cortical sliding (cf. Figs. 5 *c* and 8 *b*) but rises for the case of the combined mechanisms (cf. Fig. 10 *d*). The reason lies in the firm anchoring of MTs in the center of the IS and the emergence of the remarkable "arc" formations of attached dynein (cf. Fig. 11, *b* and *c*).

The velocity of the capture-shrinkage processes explains this surprising finding. The capture-shrinkage mechanism is more efficient because the MTs shorten because of depolymerization, align with the MTOC movement, and are pulled to the same place. Slower stepping in the cortical sliding mechanism will result in MT lengths between the MTOC and the IS far longer than the direct distance. Therefore, MTs have to bend (see Fig. 11, *e*–*g*), which explains the "arc" patterns of attached dyneins in the IS. In other words, firm anchoring of capture-shrinkage pushes the cortical sliding MTs against the IS, causing further attachment. By comparison of Fig. 5 *d* and Fig. 11 *a*, one observes that the MTOC approaches the IS more closely in the case of combined mechanisms than in the case of cortical sliding, which is another proof of the pulling of the MTOC toward the center of the IS. We conclude that the cortical sliding mechanism supports the dominant capture-shrinkage mechanism by "passing" the MTs, and the capture-shrinkage mechanism supports the cortical sliding mechanism by providing the anchoring and pushing the MTs against the IS.

This synergy is also indicated by Fig. 11 *d*, which shows the total repositioning times as a function of the density of capture-shrinkage dynein for various fixed values of the cortical sliding dynein. Although the repositioning time does not decrease further for large values of the capture-shrinkage dynein density ($\rho_{IS} > 600$ μm^{-2}), it can actually be decreased further by increasing cortical sliding dynein. Consequently, the combination of the two mechanisms with relatively low area densities is faster than the dominant mechanism alone with maximal area density (compare cases $\rho_{IS} = 200$ μm^{-2} with various $\tilde{\rho}_{IS}$ with the case of $\rho_{IS} = 1000$ μm^{-2} in Fig. 11 *d*). Further parameter variations supporting this result can be found in the Supporting Materials and

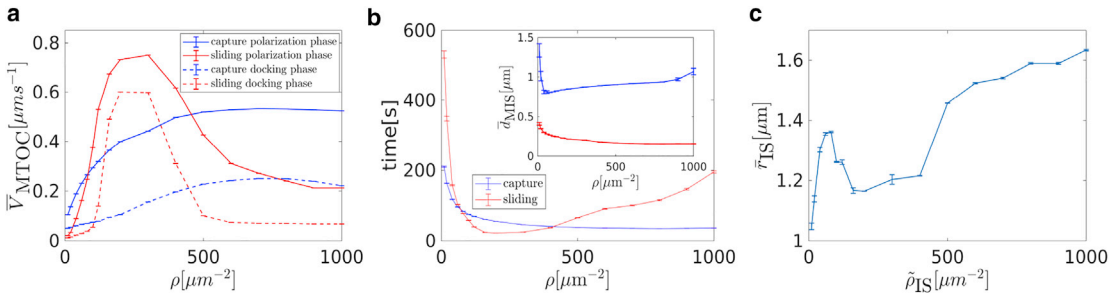

FIGURE 9 Comparison of the capture-shrinkage and the cortical sliding mechanisms in terms of the average MTOC velocity in both phases $\overline{V}_{\mathrm{MTOC}}$, times of repositioning, and the final MTOC-IS distance $\overline{d}_{\mathrm{MIS}}$. (*a*) The MTOC velocity in the first and the second phase is shown. (*b*) Repositioning times are shown. Final MTOC-IS distances are shown in the inset. (*c*) The dependence of the average distance $\bar{r}_{\mathrm{IS}}$ of attached dynein motors from the axis of the IS on dynein area density $\tilde{\rho}_{\mathrm{IS}}$ for the case of sole cortical sliding is shown. The error bars are represented by dashed lines and are plotted only if bigger than a symbol size. To see this figure in color, go online.

Methods, Section S3.3.3. The effect is certainly advantageous for the cell because the cortical sliding mechanism is not as efficient as the capture-shrinkage mechanism, considering the large amount of dynein required.

DISCUSSION

We have analyzed the experiments of (14) with a mechanistic model for the relocation of the MTOC in T cells. By using biologically realistic values for the model parameters such as the number and the stiffness of MTs, dynein pulling forces and detachment probabilities, and cytosol viscosity, we can recapitulate for a wide range of dynein densities the experimental observations of (14). In particular, the timescale for the completion of the relocation process, as well as the MTOC velocities predicted by the model, agrees well with the experimental results.

Our model predicts that the cytoskeleton deforms substantially during the MTOC-repositioning process because of the combined effects of the capture-shrinkage mechanism and friction forces. The captured MTs form a narrow stalk between the MTOC and the IS, straightening under the tension caused by dynein motors acting on it and causing the rotation of the whole MT cytoskeleton toward it. Concomitantly, unattached MTs are pushed backward by the emerging viscous drag "opening" the MT cytoskeleton (cf. Fig. 2, *e* and *f*). Thus, our model provides a mechanistic explanation of the MT cytoskeleton opening that is also

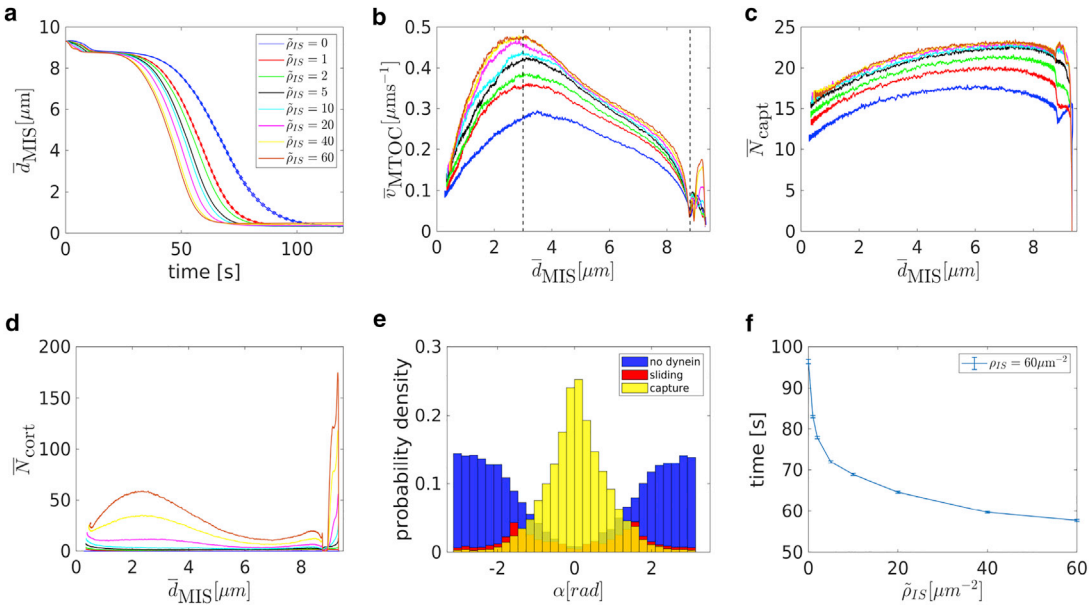

FIGURE 10 Combination of capture-shrinkage and cortical sliding: (*a*) dependence of the average MTOC-IS distance $\overline{d}_{\mathrm{MIS}}$ on time. Dependence of the average MTOC velocity $\overline{v}_{\mathrm{MTOC}}$ (*b*), the average number of attached capture-shrinkage dyneins $\overline{N}_{\mathrm{capt}}$ (*c*), and the average number of attached cortical sliding dyneins $\overline{N}_{\mathrm{cort}}$ (*d*) on the average MTOC-IS distance is shown (cortical sliding densities corresponding to different line colors in *b–d* are the same as in *a*). (*e*) The probability density of the angles α between the first MT segment and the direction of the MTOC motion is shown; $t = 50$ s, $\overline{d}_{\mathrm{MIS}} \sim 5$ μm, $\tilde{\rho}_{\mathrm{IS}} = \rho_{\mathrm{IS}} = 60$ $\mu\mathrm{m}^{-2}$. (*f*) Dependence of times of repositioning on cortical sliding area density $\tilde{\rho}_{\mathrm{IS}}$ is shown. The error bars are represented by dashed lines and are plotted only if bigger than a symbol size. To see this figure in color, go online.

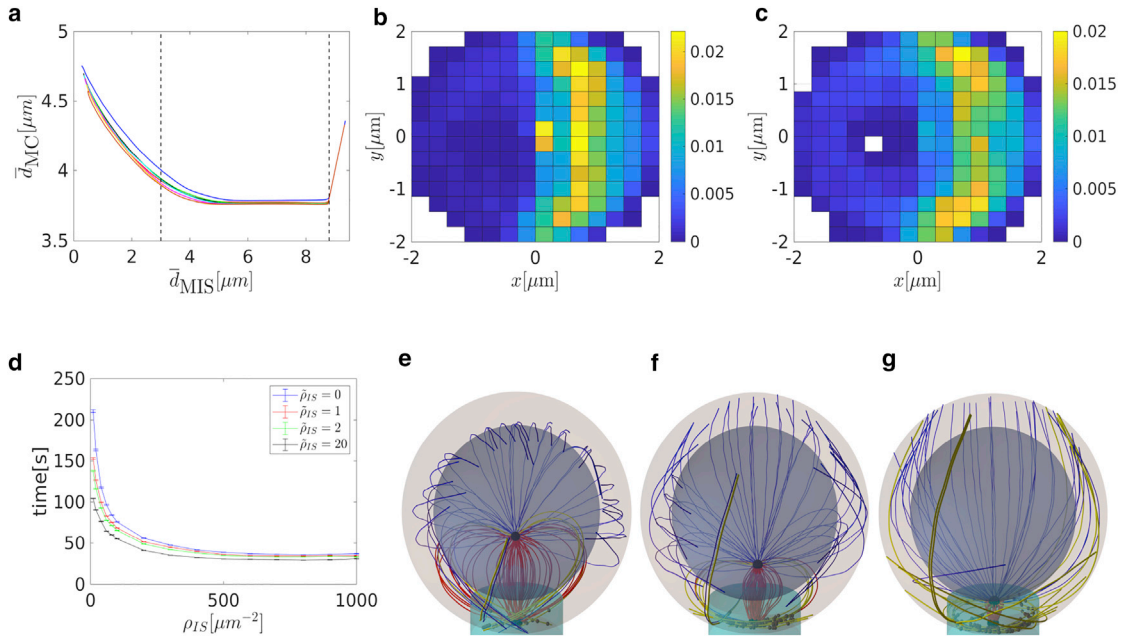

FIGURE 11 Combination of capture-shrinkage and cortical sliding. (*a*) Dependence of the average distance between the center of the cell and the MTOC $\overline{d}_{MC}$ on the average MTOC-IS distance $\overline{d}_{MIS}$ is shown. (*b* and *c*) A probability density plot for the spatial distribution of attached dynein is given. (*b*) $t = 50$ s, $\overline{d}_{MIS} \sim 4.5$ μm. (*c*) $t = 60$ s, $\overline{d}_{MIS} \sim 1.5$ μm. (*d*) Repositioning times as a function of the density of capture-shrinkage dynein ρ_{IS} for four different values of the cortical sliding area density $\tilde{\rho}_{IS}$ are shown. The error bars are represented by dashed lines and are plotted only if bigger than a symbol size. (*e–g*) Snapshots from simulation are given. The blue, red, and bold yellow curves correspond to MTs without dynein and with capture-shrinkage and cortical sliding, respectively. Black dots depict positions of attached dynein motors. (*e*) $d_{MIS} = 4.5$ μm, (*f*) $d_{MIS} = 2.5$ μm, and (*g*) $d_{MIS} = 1$ μm. To see this figure in color, go online.

clearly visible in the experiments, as, for instance, in Fig. 5 *A* of (14). The opening can also be seen in the case of combined mechanisms, although for partially different reasons (Fig. 11, *e–g*).

The MT cytoskeleton opening might have interesting consequences for the distribution of Ca^{2+} in the cell, which is highly relevant for cell function. As the cytoskeleton rotates, the mitochondria are dragged with it (16) until they approach the IS. Because of the MT cytoskeleton opening, the mitochondria are positioned asymmetrically around the IS, resulting in an asymmetric absorption and redistribution of Ca^{2+} by the mitochondria. Consequently, an asymmetric distribution of Ca^{2+} arises around the IS, the function of which might deserve further investigation.

The detailed analysis of the MT cytoskeleton arrangement for the cortical sliding mechanism revealed three different deformation characteristics depending on three regimes for the dynein density (Cortical-Sliding Mechanism). This observation opens an interesting experimental perspective to estimate the dynein distribution from the MT cytoskeleton deformation during the MTOC repositioning.

Moreover, our model also predicts a biphasic behavior of the relocation process, as reported for the experiments in (14). Figs. 3 *a* and 10 *a* bear a clear resemblance to Fig. 3 *D* of (14). We showed that after a short initial period in which MTs start to attach to the dynein, the first phase observed experimentally corresponds in our model to the circular motion of the MTOC around the nucleus and the second phase to the last 1 μm of the MTOC movement, when it detaches from the nucleus and moves more or less straight to the IS with a substantially reduced velocity for both mechanisms (capture-shrinkage and cortical sliding) and a large range of dynein densities. During the latter phase, the MTOC increases its distance from the cell center by approximately 1 μm $\sim 0.2 \times R_{Cell}$, which is close to the value reported in (14).

It was hypothesized in (14) that a resistive force emerges at the transition point between the phases, causing slowing down of the MTOC. Our model shows that the assumption of a resistive force is not necessary to explain the biphasic behavior: the velocity of the MTOC is only determined by the number of motors pulling on the MTs and on MT alignment (Figs. 3, 5 *a*, and 8). The reason for the slowing down is therefore simply the decrease of the number of dyneins attached to the MTs, which again is a consequence of the changing geometry and forces during the movement of the MTOC, i.e., a consequence of the interplay between the MT cytoskeleton and motors.

Experimentally, it was also observed that a treatment with taxol substantially reduced the velocity of the repositioning. Taxol impedes depolymerization of the MTs, which we could mimic in our model by reducing the capture-shrinkage efficiency. With this modification, our model reproduces the experimental observation (Fig. S10, *a* and *b*).

An interesting prediction of our model is that the two mechanisms, capture-shrinkage and cortical sliding, appear to act in remarkable synergy (Combination of Capture

Shrinkage and Cortical Sliding), which provides an answer to the question about the role of cortical sliding (14). Cortical sliding passes the MTs to the more efficient capture-shrinkage mechanism, which in return provides a firm anchor point. Therefore, cortical sliding is useful even in the configuration when capture-shrinkage is dominant. The synergy has a very practical effect because the combination of mechanisms with relatively low area densities can be faster than only the dominant mechanism with much higher area density Fig. 11 *d*. Therefore, the synergy of the two mechanisms can substantially reduce the area densities necessary for an effective repositioning and reduces the necessary resources (dynein). In our model, the cytoskeleton does not have to force its way through multiple organelles with complex structure, and the synergy manifests itself mainly in the velocity of the repositioning process. But one could speculate that in the real cell, the synergy can actually make the difference between completed and no repositioning.

It was proven in (50) that dyneins colocalize with the ADAP ring in the pSMAC. Moreover, in (17) it was hypothesized that the MTs are part of the reason why the pSMAC takes the form of a ring. Additionally, (17) reported the sharp turns in MTs upon interaction with the pSMAC and that the MTs do not project directly to the cSMAC. In our model, the cortical sliding dynein is homogeneously distributed over the entire IS; nevertheless, we observe that dyneins attach to MTs predominantly at the periphery of the IS (cf. Fig. 8, *d–f*). If both mechanisms are present, attached cortical sliding dyneins are even completely absent in the central region (cf. Fig. 11). We therefore conclude, like (17), that cortical sliding MTs do not project directly into the cSMAC and identify the periphery of the IS as the region where cortical sliding MTs are anchored. In agreement with the experiments (17), we observe that cortical sliding MTs turn upon contact with the periphery (Fig. 11, *e–g*), twist, and contribute to the formations of dynein "arcs." Because the dynein in the central region of the IS does not contribute to the MTOC repositioning via cortical sliding, one could hypothesize that the pSMAC takes the shape of a ring to facilitate interaction with MTs (17).

We presented a numerical analysis of the repositioning in the case in which the MTOC and the IS are initially at the opposite sides of the cell. Even a case so restricted brought interesting results, enabling comparison with experiments and a proposed explanation for the experimental observable. We found that the cell performs the repositioning with great efficiency. The dyneins are placed only at the peripheries of the IS (pSMAC), which is the place where they are used the most, evacuating less-used regions. Moreover, we introduced a synergy of two mechanisms that minimizes the necessary area density of dynein.

In this work, we presented the results of our theoretical analysis of the MTOC repositioning that are relevant for the experimental setup in (14), in which the IS and the initial position of the MTOC are diametrically opposed. Here, it turned out that even if both mechanisms (capture-shrinkage and cortical sliding) are at work, capture-shrinkage is always dominant, as reported in (14). In a second part of this work (unpublished data), we will examine other initial positions of the MTOC and the IS that will naturally occur in biologically relevant situations, and we will investigate under which circumstances cortical sliding will become the dominant mechanism over capture-shrinkage. Moreover, we will further demonstrate the synergy of two mechanisms introduced in this work and prove that it has more far-reaching effects in other initial configurations than the one studied here. Also, in the situation in which the T cell establishes two ISs, interesting dynamical behavior of the MTOC can be expected and will be analyzed in detail. In the end, we will see that in T cells the two mechanisms (capture-shrinkage and cortical sliding) and the spatial distribution of dynein are combined so as to minimize the number of dyneins necessary for polarization and to minimize the damage of the MT cytoskeleton.

SUPPORTING MATERIAL

Supporting Material can be found online at https://doi.org/10.1016/j.bpj.2020.01.045.

AUTHOR CONTRIBUTIONS

H.R. designed the research. I.H. performed calculations, prepared figures, and analyzed the data. I.H. and H.R. wrote the manuscript.

ACKNOWLEDGMENTS

The authors thank Bin Qu and Renping Zhao for helpful discussions.

This work was financially supported by the German Research Foundation within the Collaborative Research Center SFB 1027.

SUPPORTING CITATIONS

References (76–130) appear in the Supporting Material.

REFERENCES

1. Rudolph, M. G., R. L. Stanfield, and I. A. Wilson. 2006. How TCRs bind MHCs, peptides, and coreceptors. *Annu. Rev. Immunol.* 24:419–466.
2. Garcia, K. C. 2012. Reconciling views on T cell receptor germline bias for MHC. *Trends Immunol.* 33:429–436.
3. Zinkernagel, R. M., and P. C. Doherty. 1974. Restriction of in vitro T cell-mediated cytotoxicity in lymphocytic choriomeningitis within a syngeneic or semiallogeneic system. *Nature.* 248:701–702.
4. Attaf, M., M. Legut, …, A. K. Sewell. 2015. The T cell antigen receptor: the Swiss army knife of the immune system. *Clin. Exp. Immunol.* 181:1–18.
5. Wucherpfennig, K. W. 2004. T cell receptor crossreactivity as a general property of T cell recognition. *Mol. Immunol.* 40:1009–1017.
6. Babbitt, B. P., P. M. Allen, …, E. R. Unanue. 1985. Binding of immunogenic peptides to Ia histocompatibility molecules. *Nature.* 317:359–361.

7. Monks, C. R., B. A. Freiberg, …, A. Kupfer. 1998. Three-dimensional segregation of supramolecular activation clusters in T cells. *Nature.* 395:82–86.

8. Dustin, M. L., M. W. Olszowy, …, A. S. Shaw. 1998. A novel adaptor protein orchestrates receptor patterning and cytoskeletal polarity in T-cell contacts. *Cell.* 94:667–677.

9. Dustin, M. L., A. K. Chakraborty, and A. S. Shaw. 2010. Understanding the structure and function of the immunological synapse. *Cold Spring Harb. Perspect. Biol.* 2:a002311.

10. Huang, Y., D. D. Norton, …, R. L. Wange. 2005. Deficiency of ADAP/Fyb/SLAP-130 destabilizes SKAP55 in Jurkat T cells. *J. Biol. Chem.* 280:23576–23583.

11. André, P., A. M. Benoliel, …, P. Bongrand. 1990. Use of conjugates made between a cytolytic T cell clone and target cells to study the redistribution of membrane molecules in cell contact areas. *J. Cell Sci.* 97:335–347.

12. Geiger, B., D. Rosen, and G. Berke. 1982. Spatial relationships of microtubule-organizing centers and the contact area of cytotoxic T lymphocytes and target cells. *J. Cell Biol.* 95:137–143.

13. Kupfer, A., D. Louvard, and S. J. Singer. 1982. Polarization of the Golgi apparatus and the microtubule-organizing center in cultured fibroblasts at the edge of an experimental wound. *Proc. Natl. Acad. Sci. USA.* 79:2603–2607.

14. Yi, J., X. Wu, …, J. A. Hammer. 2013. Centrosome repositioning in T cells is biphasic and driven by microtubule end-on capture-shrinkage. *J. Cell Biol.* 202:779–792.

15. Stinchcombe, J. C., E. Majorovits, …, G. M. Griffiths. 2006. Centrosome polarization delivers secretory granules to the immunological synapse. *Nature.* 443:462–465.

16. Maccari, I., R. Zhao, …, H. Rieger. 2016. Cytoskeleton rotation relocates mitochondria to the immunological synapse and increases calcium signals. *Cell Calcium.* 60:309–321.

17. Kuhn, J. R., and M. Poenie. 2002. Dynamic polarization of the microtubule cytoskeleton during CTL-mediated killing. *Immunity.* 16:111–121.

18. Hui, K. L., and A. Upadhyaya. 2017. Dynamic microtubules regulate cellular contractility during T-cell activation. *Proc. Natl. Acad. Sci. USA.* 114:E4175–E4183.

19. Kupfer, A., and G. Dennert. 1984. Reorientation of the microtubule-organizing center and the Golgi apparatus in cloned cytotoxic lymphocytes triggered by binding to lysable target cells. *J. Immunol.* 133:2762–2766.

20. Kupfer, A., S. L. Swain, …, S. J. Singer. 1986. The specific direct interaction of helper T cells and antigen-presenting B cells. *Proc. Natl. Acad. Sci. USA.* 83:6080–6083.

21. Gurel, P. S., A. L. Hatch, and H. N. Higgs. 2014. Connecting the cytoskeleton to the endoplasmic reticulum and Golgi. *Curr. Biol.* 24:R660–R672.

22. Lee, C., and L. B. Chen. 1988. Dynamic behavior of endoplasmic reticulum in living cells. *Cell.* 54:37–46.

23. Waterman-Storer, C. M., and E. D. Salmon. 1998. Endoplasmic reticulum membrane tubules are distributed by microtubules in living cells using three distinct mechanisms. *Curr. Biol.* 8:798–806.

24. Palmer, K. J., P. Watson, and D. J. Stephens. 2005. The role of microtubules in transport between the endoplasmic reticulum and Golgi apparatus in mammalian cells. *Biochem. Soc. Symp.* 72:1–13.

25. Müllbacher, A., P. Waring, …, M. M. Simon. 1999. Granzymes are the essential downstream effector molecules for the control of primary virus infections by cytolytic leukocytes. *Proc. Natl. Acad. Sci. USA.* 96:13950–13955.

26. Lowin, B., M. C. Peitsch, and J. Tschopp. 1995. Perforin and granzymes: crucial effector molecules in cytolytic T lymphocyte and natural killer cell-mediated cytotoxicity. *Curr. Top. Microbiol. Immunol.* 198:1–24.

27. Voskoboinik, I., M. J. Smyth, and J. A. Trapani. 2006. Perforin-mediated target-cell death and immune homeostasis. *Nat. Rev. Immunol.* 6:940–952.

28. Grossman, W. J., P. A. Revell, …, T. J. Ley. 2003. The orphan granzymes of humans and mice. *Curr. Opin. Immunol.* 15:544–552.

29. Krzewski, K., and J. E. Coligan. 2012. Human NK cell lytic granules and regulation of their exocytosis. *Front. Immunol.* 3:335.

30. Yannelli, J. R., J. A. Sullivan, …, V. H. Engelhard. 1986. Reorientation and fusion of cytotoxic T lymphocyte granules after interaction with target cells as determined by high resolution cinemicrography. *J. Immunol.* 136:377–382.

31. Pasternack, M. S., C. R. Verret, …, H. N. Eisen. 1986. Serine esterase in cytolytic T lymphocytes. *Nature.* 322:740–743.

32. Poo, W. J., L. Conrad, and C. A. Janeway, Jr. 1988. Receptor-directed focusing of lymphokine release by helper T cells. *Nature.* 332:378–380.

33. Kupfer, H., C. R. Monks, and A. Kupfer. 1994. Small splenic B cells that bind to antigen-specific T helper (Th) cells and face the site of cytokine production in the Th cells selectively proliferate: immunofluorescence microscopic studies of Th-B antigen-presenting cell interactions. *J. Exp. Med.* 179:1507–1515.

34. Stinchcombe, J. C., G. Bossi, …, G. M. Griffiths. 2001. The immunological synapse of CTL contains a secretory domain and membrane bridges. *Immunity.* 15:751–761.

35. Haddad, E. K., X. Wu, …, P. A. Henkart. 2001. Defective granule exocytosis in Rab27a-deficient lymphocytes from Ashen mice. *J. Cell Biol.* 152:835–842.

36. Griffiths, G. M. 1997. Protein sorting and secretion during CTL killing. *Semin. Immunol.* 9:109–115.

37. Stinchcombe, J. C., D. C. Barral, …, G. M. Griffiths. 2001. Rab27a is required for regulated secretion in cytotoxic T lymphocytes. *J. Cell Biol.* 152:825–834.

38. Calvo, V., and M. Izquierdo. 2018. Imaging polarized secretory traffic at the immune synapse in living T lymphocytes. *Front. Immunol.* 9:684.

39. Kupfer, A., G. Dennert, and S. J. Singer. 1985. The reorientation of the Golgi apparatus and the microtubule-organizing center in the cytotoxic effector cell is a prerequisite in the lysis of bound target cells. *J. Mol. Cell. Immunol.* 2:37–49.

40. Golstein, P., and G. M. Griffiths. 2018. An early history of T cell-mediated cytotoxicity. *Nat. Rev. Immunol.* 18:527–535.

41. Bertrand, F., S. Müller, …, S. Valitutti. 2013. An initial and rapid step of lytic granule secretion precedes microtubule organizing center polarization at the cytotoxic T lymphocyte/target cell synapse. *Proc. Natl. Acad. Sci. USA.* 110:6073–6078.

42. Lin, J., M. J. Miller, and A. S. Shaw. 2005. The c-SMAC: sorting it all out (or in). *J. Cell Biol.* 170:177–182.

43. Choudhuri, K., and M. L. Dustin. 2010. Signaling microdomains in T cells. *FEBS Lett.* 584:4823–4831.

44. Hammer, J. A., J. C. Wang, …, A. T. Pedrosa. 2019. Origin, organization, dynamics, and function of actin and actomyosin networks at the T cell immunological synapse. *Annu. Rev. Immunol.* 37:201–224.

45. Martín-Cófreces, N. B., J. Robles-Valero, …, F. Sánchez-Madrid. 2008. MTOC translocation modulates IS formation and controls sustained T cell signaling. *J. Cell Biol.* 182:951–962.

46. Nguyen-Ngoc, T., K. Afshar, and P. Gönczy. 2007. Coupling of cortical dynein and G α proteins mediates spindle positioning in *Caenorhabditis* elegans. *Nat. Cell Biol.* 9:1294–1302.

47. Saito, T. T., D. Okuzaki, and H. Nojima. 2006. Mcp5, a meiotic cell cortex protein, is required for nuclear movement mediated by dynein and microtubules in fission yeast. *J. Cell Biol.* 173:27–33.

48. Yamashita, A., and M. Yamamoto. 2006. Fission yeast Num1p is a cortical factor anchoring dynein and is essential for the horse-tail nuclear movement during meiotic prophase. *Genetics.* 173:1187–1196.

49. Ananthanarayanan, V., M. Schattat, …, I. M. Tolić-Nørrelykke. 2013. Dynein motion switches from diffusive to directed upon cortical anchoring. *Cell.* 153:1526–1536.

50. Combs, J., S. J. Kim, …, M. Poenie. 2006. Recruitment of dynein to the Jurkat immunological synapse. *Proc. Natl. Acad. Sci. USA.* 103:14883–14888.

51. Hashimoto-Tane, A., T. Yokosuka, …, T. Saito. 2011. Dynein-driven transport of T cell receptor microclusters regulates immune synapse formation and T cell activation. *Immunity.* 34:919–931.

52. Stinchcombe, J. C., and G. M. Griffiths. 2014. Communication, the centrosome and the immunological synapse. *Philos. Trans. R. Soc. Lond. B Biol. Sci.* 369:20130463.

53. Quann, E. J., E. Merino, …, M. Huse. 2009. Localized diacylglycerol drives the polarization of the microtubule-organizing center in T cells. *Nat. Immunol.* 10:627–635.

54. Laan, L., N. Pavin, …, M. Dogterom. 2012. Cortical dynein controls microtubule dynamics to generate pulling forces that position microtubule asters. *Cell.* 148:502–514.

55. Breart, B., F. Lemaître, …, P. Bousso. 2008. Two-photon imaging of intratumoral CD8+ T cell cytotoxic activity during adoptive T cell therapy in mice. *J. Clin. Invest.* 118:1390–1397.

56. He, J.-S., and H. L. Ostergaard. 2007. CTLs contain and use intracellular stores of FasL distinct from cytolytic granules. *J. Immunol.* 179:2339–2348.

57. Kim, M. J., and I. V. Maly. 2009. Deterministic mechanical model of T-killer cell polarization reproduces the wandering of aim between simultaneously engaged targets. *PLoS Comput. Biol.* 5:e1000260.

58. Sarkar, A., H. Rieger, and R. Paul. 2019. Search and capture efficiency of dynamic microtubules for centrosome relocation during IS formation. *Biophys. J.* 116:2079–2091.

59. Cooper, G. M. 2000. The Cell: A Molecular Approach, Second Edition. Sinauer Associates, Sunderland, MA.

60. Li, H., D. J. DeRosier, …, K. H. Downing. 2002. Microtubule structure at 8 A resolution. *Structure.* 10:1317–1328.

61. Meurer-Grob, P., J. Kasparian, and R. H. Wade. 2001. Microtubule structure at improved resolution. *Biochemistry.* 40:8000–8008.

62. Jia, K., and X. Liu. 2017. Measuring the flexural rigidity of actin filaments and microtubules from their thermal fluctuating shapes: a new perspective. *J. Mech. Phys. Solids.* 101:64–92.

63. Takasone, T., S. Juodkazis, …, H. Misawa. 2002. Flexural rigidity of a single microtubule. *Jpn. J. Appl. Phys.* 41:3015–3019.

64. Gittes, F., B. Mickey, …, J. Howard. 1993. Flexural rigidity of microtubules and actin filaments measured from thermal fluctuations in shape. *J. Cell Biol.* 120:923–934.

65. Broedersz, C., and F. MacKintosh. 2014. Modeling semiflexible polymer networks. *Rev. Mod. Phys.* 86:995–1036.

66. Chrétien, D., B. Buendia, …, E. Karsenti. 1997. Reconstruction of the centrosome cycle from cryoelectron micrographs. *J. Struct. Biol.* 120:117–133.

67. Winey, M., and E. O'Toole. 2014. Centriole structure. *Philos. Trans. R. Soc. Lond. B Biol. Sci.* 369:20130457.

68. Guichard, P., V. Hachet, …, P. Gönczy. 2013. Native architecture of the centriole proximal region reveals features underlying its 9-fold radial symmetry. *Curr. Biol.* 23:1620–1628.

69. Bernhard, W., and E. De Harven. 1956. Electron microscopic study of the ultrastructure of centrioles in vertebra. *Z. Zellforsch. Mikrosk. Anat.* 45:378–398.

70. Woodruff, J. B., O. Wueseke, and A. A. Hyman. 2014. Pericentriolar material structure and dynamics. *Philos. Trans. R. Soc. Lond. B Biol. Sci.* 369:20130459.

71. Moritz, M., M. B. Braunfeld, …, D. A. Agard. 2000. Structure of the gamma-tubulin ring complex: a template for microtubule nucleation. *Nat. Cell Biol.* 2:365–370.

72. Robbins, E., G. Jentzsch, and A. Micali. 1968. The centriole cycle in synchronized HeLa cells. *J. Cell Biol.* 36:329–339.

73. Moritz, M., M. B. Braunfeld, …, D. A. Agard. 1995. Microtubule nucleation by gamma-tubulin-containing rings in the centrosome. *Nature.* 378:638–640.

74. Burgess, S. A., M. L. Walker, …, K. Oiwa. 2003. Dynein structure and power stroke. *Nature.* 421:715–718.

75. Belyy, V., M. A. Schlager, …, A. Yildiz. 2016. The mammalian dynein-dynactin complex is a strong opponent to kinesin in a tug-of-war competition. *Nat. Cell Biol.* 18:1018–1024.

76. Puchkov, E. O. 2013. Intracellular viscosity: methods of measurement and role in metabolism. *Biochem. Moscow Suppl. Ser. A.* 7:270–279.

77. Bausch, A. R., W. Möller, and E. Sackmann. 1999. Measurement of local viscoelasticity and forces in living cells by magnetic tweezers. *Biophys. J.* 76:573–579.

78. Howard, J. 2001. Mechanics of Motor Proteins and the Cytoskeleton. Sinauer Associates, Sunderland, MA.

79. Leith, D. 1987. Drag on nonspherical objects. *Aerosol Sci. Technol.* 6:153–161.

80. Bereiter-Hahn, J., and M. Vöth. 1994. Dynamics of mitochondria in living cells: shape changes, dislocations, fusion, and fission of mitochondria. *Microsc. Res. Tech.* 27:198–219.

81. Jakobs, S. 2006. High resolution imaging of live mitochondria. *Biochim. Biophys. Acta.* 1763:561–575.

82. Chaudhuri, A. 2016. Cell biology by the numbers. *Yale J. Biol. Med.* 89:425–426.

83. Fawcett, D. W. 1966. An atlas of fine structure. The cell. Its organelles and inclusions. *Ann. Intern. Med.* 64:968.

84. Jakobs, S., and C. A. Wurm. 2014. Super-resolution microscopy of mitochondria. *Curr. Opin. Chem. Biol.* 20:9–15.

85. Xu, H., W. Su, …, H. Wang. 2013. The asymmetrical structure of Golgi apparatus membranes revealed by in situ atomic force microscope. *PLoS One.* 8:e61596.

86. Ladinsky, M. S., D. N. Mastronarde, …, L. A. Staehelin. 1999. Golgi structure in three dimensions: functional insights from the normal rat kidney cell. *J. Cell Biol.* 144:1135–1149.

87. Day, K. J., L. A. Staehelin, and B. S. Glick. 2013. A three-stage model of Golgi structure and function. *Histochem. Cell Biol.* 140:239–249.

88. Huang, S., and Y. Wang. 2017. Golgi structure formation, function, and post-translational modifications in mammalian cells. *F1000 Res.* 6:2050.

89. Westrate, L. M., J. E. Lee, …, G. K. Voeltz. 2015. Form follows function: the importance of endoplasmic reticulum shape. *Annu. Rev. Biochem.* 84:791–811.

90. English, A. R., and G. K. Voeltz. 2013. Endoplasmic reticulum structure and interconnections with other organelles. *Cold Spring Harb. Perspect. Biol.* 5:a013227.

91. English, A. R., N. Zurek, and G. K. Voeltz. 2009. Peripheral ER structure and function. *Curr. Opin. Cell Biol.* 21:596–602.

92. Shibata, Y., G. K. Voeltz, and T. A. Rapoport. 2006. Rough sheets and smooth tubules. *Cell.* 126:435–439.

93. Hu, J., W. A. Prinz, and T. A. Rapoport. 2011. Weaving the web of ER tubules. *Cell.* 147:1226–1231.

94. Alberts, B., A. Johnson, …, P. Walter. 2007. Molecular Biology of the Cell, Fifth Edition. Garland Science, New York.

95. Goodenough, U. W., B. Gebhart, …, J. E. Heuser. 1987. High-pressure liquid chromatography fractionation of Chlamydomonas dynein extracts and characterization of inner-arm dynein subunits. *J. Mol. Biol.* 194:481–494.

96. Gee, M. A., J. E. Heuser, and R. B. Vallee. 1997. An extended microtubule-binding structure within the dynein motor domain. *Nature.* 390:636–639.

97. Goodenough, U., and J. Heuser. 1984. Structural comparison of purified dynein proteins with in situ dynein arms. *J. Mol. Biol.* 180:1083–1118.

98. Schmidt, H., E. S. Gleave, and A. P. Carter. 2012. Insights into dynein motor domain function from a 3.3-Å crystal structure. *Nat. Struct. Mol. Biol.* 19:492–497, S1.

99. Leduc, C., O. Campàs, …, J. Prost. 2004. Cooperative extraction of membrane nanotubes by molecular motors. *Proc. Natl. Acad. Sci. USA.* 101:17096–17101.

100. Kamiya, N., T. Mashimo, …, H. Nakamura. 2016. Elastic properties of dynein motor domain obtained from all-atom molecular dynamics simulations. *Protein Eng. Des. Sel.* 29:317–325.

101. Lindemann, C. B., and A. J. Hunt. 2003. Does axonemal dynein push, pull, or oscillate? *Cell Motil. Cytoskeleton.* 56:237–244.

102. Sakakibara, H., H. Kojima, …, K. Oiwa. 1999. Inner-arm dynein c of Chlamydomonas flagella is a single-headed processive motor. *Nature.* 400:586–590.

103. Sakakibara, H., and K. Oiwa. 2011. Molecular organization and force-generating mechanism of dynein. *FEBS J.* 278:2964–2979.

104. Gennerich, A., A. P. Carter, …, R. D. Vale. 2007. Force-induced bidirectional stepping of cytoplasmic dynein. *Cell.* 131:952–965.

105. Toba, S., T. M. Watanabe, …, H. Higuchi. 2006. Overlapping hand-over-hand mechanism of single molecular motility of cytoplasmic dynein. *Proc. Natl. Acad. Sci. USA.* 103:5741–5745.

106. Mallik, R., D. Petrov, …, S. P. Gross. 2005. Building complexity: an in vitro study of cytoplasmic dynein with in vivo implications. *Curr. Biol.* 15:2075–2085.

107. Mallik, R., B. C. Carter, …, S. P. Gross. 2004. Cytoplasmic dynein functions as a gear in response to load. *Nature.* 427:649–652.

108. Reck-Peterson, S. L., A. Yildiz, …, R. D. Vale. 2006. Single-molecule analysis of dynein processivity and stepping behavior. *Cell.* 126:335–348.

109. Kural, C., H. Kim, …, P. R. Selvin. 2005. Kinesin and dynein move a peroxisome in vivo: a tug-of-war or coordinated movement? *Science.* 308:1469–1472.

110. Torisawa, T., M. Ichikawa, …, K. Furuta. 2014. Autoinhibition and cooperative activation mechanisms of cytoplasmic dynein. *Nat. Cell Biol.* 16:1118–1124.

111. Müller, M. J. I., S. Klumpp, and R. Lipowsky. 2008. Tug-of-war as a cooperative mechanism for bidirectional cargo transport by molecular motors. *Proc. Natl. Acad. Sci. USA.* 105:4609–4614.

112. King, S. J., and T. A. Schroer. 2000. Dynactin increases the processivity of the cytoplasmic dynein motor. *Nat. Cell Biol.* 2:20–24.

113. Nishiura, M., T. Kon, …, K. Sutoh. 2004. A single-headed recombinant fragment of Dictyostelium cytoplasmic dynein can drive the robust sliding of microtubules. *J. Biol. Chem.* 279:22799–22802.

114. Kon, T., M. Nishiura, …, K. Sutoh. 2004. Distinct functions of nucleotide-binding/hydrolysis sites in the four AAA modules of cytoplasmic dynein. *Biochemistry.* 43:11266–11274.

115. Cho, C., S. L. Reck-Peterson, and R. D. Vale. 2008. Regulatory ATPase sites of cytoplasmic dynein affect processivity and force generation. *J. Biol. Chem.* 283:25839–25845.

116. Kikushima, K., T. Yagi, and R. Kamiya. 2004. Slow ADP-dependent acceleration of microtubule translocation produced by an axonemal dynein. *FEBS Lett.* 563:119–122.

117. Walter, W. J., B. Brenner, and W. Steffen. 2010. Cytoplasmic dynein is not a conventional processive motor. *J. Struct. Biol.* 170:266–269.

118. Ikuta, J., N. K. Kamisetty, …, R. Yokokawa. 2014. Tug-of-war of microtubule filaments at the boundary of a kinesin- and dynein-patterned surface. *Sci. Rep.* 4:5281.

119. Kunwar, A., S. K. Tripathy, …, S. P. Gross. 2011. Mechanical stochastic tug-of-war models cannot explain bidirectional lipid-droplet transport. *Proc. Natl. Acad. Sci. USA.* 108:18960–18965.

120. Klein, S., C. Appert-Rolland, and L. Santen. 2015. Motility states in bidirectional cargo transport. *EPL.* 111:68005.

121. Roberts, A. J., N. Numata, …, S. A. Burgess. 2009. AAA+ Ring and linker swing mechanism in the dynein motor. *Cell.* 136:485–495.

122. Imai, H., T. Shima, …, S. A. Burgess. 2015. Direct observation shows superposition and large scale flexibility within cytoplasmic dynein motors moving along microtubules. *Nat. Commun.* 6:8179.

123. Mizuno, N., A. Narita, …, M. Kikkawa. 2007. Three-dimensional structure of cytoplasmic dynein bound to microtubules. *Proc. Natl. Acad. Sci. USA.* 104:20832–20837.

124. Montesi, A., D. C. Morse, and M. Pasquali. 2005. Brownian dynamics algorithm for bead-rod semiflexible chain with anisotropic friction. *J. Chem. Phys.* 122:84903.

125. Fixman, M. 1978. Simulation of polymer dynamics. I. General theory. *J. Chem. Phys.* 69:1527–1537.

126. Hinch, E. J. 1994. Brownian motion with stiff bonds and rigid constraints. *J. Fluid Mech.* 271:219–234.

127. Grassia, P. S., E. J. Hinch, and L. C. Nitsche. 1995. Computer simulations of Brownian motion of complex systems. *J. Fluid Mech.* 282:373–403.

128. Grassia, P., and E. J. Hinch. 1996. Computer simulations of polymer chain relaxation via Brownian motion. *J. Fluid Mech.* 308:255–288.

129. Pasquali, M., and D. C. Morse. 2002. An efficient algorithm for metric correction forces in simulations of linear polymers with constrained bond lengths. *J. Chem. Phys.* 116:1834–1838.

130. Nedelec, F., and D. Foethke. 2007. Collective Langevin dynamics of flexible cytoskeletal fibers. *New J. Phys.* 9:427.

Biophysical Journal, Volume *118*

Supplemental Information

Stochastic Model of T Cell Repolarization during Target Elimination I

Ivan Hornak and Heiko Rieger

Stochastic model of T Cell repolarization during target elimination (I) SUPPLEMENTARY MATERIAL

Ivan Hornak, Heiko Rieger

1 Model of the cell

1.1 Microtubules

The microtubules(MTs) are represented as semiflexible filaments, therefore the Hamiltonian of a single MT is given by:

$$H = \frac{\kappa}{2} \int_0^L \left| \frac{\partial \vec{t}}{\partial s} \right|^2, \tag{1}$$

where κ is bending rigidity($2.2 * 10^{-23}\text{Nm}^2$), L is the length of MT, s is arc length, $\vec{t} = \frac{\partial \vec{r}}{\partial s}$ is unit tangent vector and $\vec{r}(s)$ is a position (1). A single MT is represented as a chain of N beads with coordinates $\vec{r}_1, ..., \vec{r}_N$ connected by $N-1$ tangents $\vec{ti} = \vec{r}_{i+1} - \vec{r}_i$ of the length $k = L/(N-1)$. In the present model, the length $k = 0.8\mu$m was used. Since the MT is an inextensible polymer discretized into N beads, $N-1$ constraints must be fulfilled:

$$C_i^{\text{micro}} = |\vec{r}_i - \vec{r}_{i+1}| = k \qquad\qquad i = 1, ..., N-1 \tag{2}$$

The length of the MTs varies considerably, but since short MTs are not relevant for repositioning, we include only just MTs that reach from the MTOC to the IS in the first seconds of repositioning. The maximum length of a MT should be $L > \pi * R_{\text{Cell}}$ to always reach from MTOC to IS. In order to reach the IS in the first stages of repolarization, the length must be $L > \frac{3}{4} * \pi * R_{\text{Cell}}$. Thus, the number of beads N is uniformly distributed between 15 and 20.

1.1.1 Bending forces of the microtubule

The Hamiltonian for the discretized MT can be expressed as:

$$H_{bend} = \kappa_d \sum_{i=0}^{N-2} \left(1 - \frac{\vec{t}_i \vec{t}_{i+1}}{|\vec{t}_i||\vec{t}_{i+1}|} \right), \tag{3}$$

where $\kappa_d = \kappa/k$ is the bending rigidity of the discretized model. The bending force acting on bead i is the derivative of the discretized Hamiltonian with the respect to $\vec{r}_i$:

$$\vec{F}_i^{\text{bend}} = -\frac{\partial H_{bend}}{\partial \vec{r}_i}. \tag{4}$$

If we consider the simplest case (sketched in Fig. 2) of three points with coordinates $\vec{r}_1$, $\vec{r}_2$ and $\vec{r}_3$ connected with the tangents $\vec{t}_1$ and $\vec{t}_2$, the bending forces acting on the beads are:

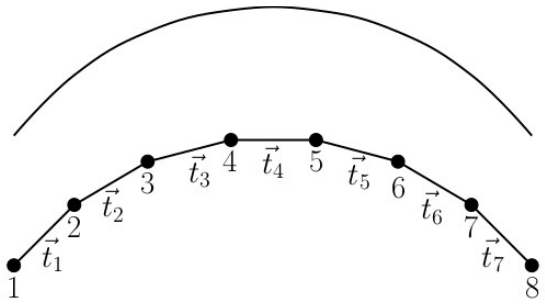

Figure 1: Bead-rod model of the microtubule. The MT is divided into 8 point connected by 7 rods. The circles correspond to the positions of the beads. The lengths of rods connecting beads remain constant.

$$\vec{F}_1^{\text{bend}} = \frac{\kappa_d}{|\vec{t}_1|} \left(-\frac{\vec{t}_2}{|\vec{t}_2|} + \frac{\vec{t}_1}{|\vec{t}_1|} \left(\frac{\vec{t}_1 \cdot \vec{t}_2}{|\vec{t}_2||\vec{t}_1|} \right) \right), \tag{5a}$$

$$\vec{F}_3^{\text{bend}} = \frac{\kappa_d}{|\vec{t}_2|} \left(\frac{\vec{t}_1}{|\vec{t}_1|} - \frac{\vec{t}_2}{|\vec{t}_2|} \left(\frac{\vec{t}_1 \cdot \vec{t}_2}{|\vec{t}_2||\vec{t}_1|} \right) \right) \tag{5b}$$

$$\vec{F}_2^{\text{bend}} = -\vec{F}_3^{\text{bend}} - \vec{F}_1^{\text{bend}}. \tag{5c}$$

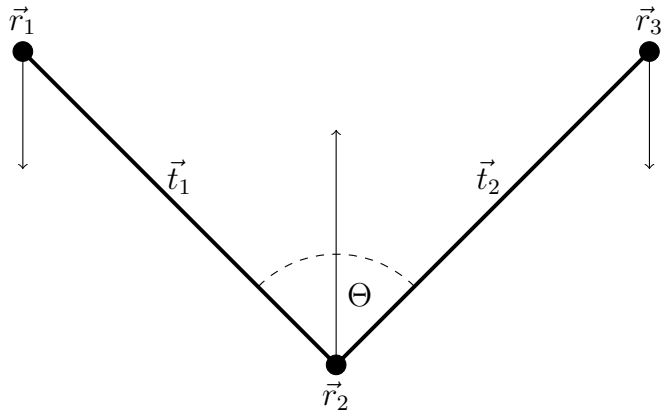

Figure 2: The sketch of bending forces acting on the MT composed of three beads. The filled circles represent the beads of the MT. The bending force is determined by the angle Θ between the tangents $\vec{t}_1$ and $\vec{t}_2$. The narrow arows depict bending forces acting on beads.

1.1.2 Drag coefficient

The drag force on an object depends on the speed of the object, the viscosity μ of the fluid, the size, and the shape of the object. The intracellular viscosity is very hard to measure or estimate, since the space between the nucleus and cell membrane is far from homogenous. The viscosity of aqueous domains of cell cytoplasm corresponds to the viscosity of water (2). On the other hand, in other microdomains, the local viscosity differs from the viscosity of water by more than three orders of magnitude (3). The effective viscosity in our model was chosen as:

$$\mu \sim 30\mu\mathrm{w} = 0.03\mathrm{Pa}\cdot\mathrm{s}, \tag{6}$$

where $\mu_\mathrm{w} = 0.9775\mathrm{mPa}\cdot\mathrm{s}$ is the viscosity of water at temperature of $T = 21°\mathrm{C}$.

The MT is divided into segments of a cylindrical shape whose length is substantially bigger than the diameter. The drag depends on the object's area projected normal to the direction of the motion. Therefore, drag forces for the motions parallel and perpendicular to the object are defined as $F = \gamma_\parallel \dot{x}$ and $F = \gamma_\perp \dot{x}$, respectively, where $\dot{x}$ is speed of the object. Parallel $\gamma_\parallel$ and perpendicular $\gamma_\perp$ drag coefficients (4) are defined for the case of a cylinder in the fluid with viscosity μ as:

$$\gamma_\parallel = \frac{2\pi\mu k}{\ln(k/d) - 0.2} \tag{7a}$$

$$\gamma_\perp = \frac{4\pi\mu k}{\ln(k/d) + 0.84}, \tag{7b}$$

where k and d are the length and the diameter of the cylinder, respectively. Therefore, the friction of the cylinder is anisotropic $\gamma_\perp \sim 2\gamma_\parallel$. However, the anisotropy is hard to implement, as the orientation of segments varies. Therefore, the anisotropy is not implemented. For the case of simplicity, the perpendicular drag coefficient is considered in the simulation to the beads of MT and the same drag coefficient is attributed to all MTOC points.

1.2 Drag force of organelles

EM, Golgi and mitochondria are the organelles with different structures and sizes. However, their drag force can be estimated from their volume and surfaces. A dynamic shape factor(5), K_sf, can be defined to calculate the drag coefficient of the nonspherical particle:

$$\gamma = 3\pi d_v \mu K_\mathrm{sf}, \tag{8}$$

where d_v is the diameter of the sphere with the same volume as the object. The drag force can be divided between the form drag, coming from the pressure on the surface, and tangential shear stress. Form drag is determined by the objects area projected normal to the direction of the motion. It can be expressed through the Stokes law form drag on a sphere, whose projected area equals to the projected area of a nonspherical object. The diameter of such a sphere is d_n. The friction force on the surface can be expressed by the friction on the sphere with the same effective surface, which has the diameter d_s. The dynamic shape factor can be defined as:

$$K_\mathrm{sf} = \frac{d_n + 2d_s}{3d_v}. \tag{9}$$

The number of mitochondria were measured(just the case of one cell) in (6) (44 mitochondria in a T-Cell). The size and shape of MTs varies greatly, since they can shrink, grow, go through fission and fusion (7–11). We consider the

most common spherocylindrical shape approximated by the cylinder, whose diameter and the length were estimated as 0.75μm and 1.5μm, respectively. Golgi apparatus is a very complex structure composed from multiple classes of cisternae differing in form, function and composition that are stacked in various ways (12–15). The endoplasmic reticulum (ER) is also a complex organelle composed from a bilayer forming nuclear envelope and a network of sheets and dynamic tubules (16–20). Golgi, ER and mitochondria are connected to cytoskeleton (21) and (6).

For the rough approximate evaluation of drag force we consider the estimates from (22), table 12. The major organelles including EM and Golgi are close to the center and they are in contact. Consequently, effective viscosity in the regions close to the nucleus of the cell is different from more aqueous domain close to the cell membrane where the rotation of the cytoskeleton takes place. Therefore, we assume that the effective viscosity of the medium in which EM and Golgi travel is $\mu_2 = 10 * \mu$. We will express the drag coefficient of organelles as a function of viscosity and compare it with the drag coefficient of the cytoskeleton. For the estimate of the cytoskeleton drag coefficient, the cytoskeleton of 100 MTs was considered and the drag coefficient were calculated using (9).

$$\gamma_{\text{GSER}} \sim 0.00131\mu \tag{10}$$
$$\gamma_{\text{RER}} \sim 0.00160\mu \tag{11}$$
$$\gamma_{\text{Mito}} \sim 0.00257\mu \tag{12}$$
$$\gamma_{\text{Cyto}} \sim 0.00270\mu \tag{13}$$

From the equations (10) it can be seen that the $\gamma_{\text{total}} = (\gamma_{\text{Cyto}} + \gamma_{\text{Mito}} + \gamma_{\text{RER}} + \gamma_{\text{GSER}}) \sim 3 * \gamma_{\text{Cyto}}$. Consequently, to consider the drag force from the organelles in the cell, the drag coefficient of MT is tripled. Thus, the equation (7) can be rewritten as:

$$\gamma_{\parallel} = 3 * \frac{2\pi\mu k}{\ln(k/d) - 0.2} \tag{14a}$$
$$\gamma_{\perp} = 3 * \frac{4\pi\mu k}{\ln(k/d) + 0.84}. \tag{14b}$$

1.3 Confinement of the cytoskeleton

The cytoskeleton moves between the wall of the cell and the nucleus. They have a spherical shape and they are modeled as force fields. The force of the wall is null if $|\vec{r}_i| <= R$. Otherwise, the force acting on the bead of the MT or the MTOC is expressed as:

$$\vec{F}_i^{\text{wall}} = -1\frac{\vec{r}_i}{|\vec{r}_i|}k_1\text{exp}(k_2(|\vec{r}_i| - R)), \tag{15}$$

where R is the radius of the cell and $k_1 = 20\text{pN}\mu\text{m}^{-1}$ and $k_2 = 1\text{m}^{-1}$ are chosen constants. The force of nucleus is null if $|\vec{r}_i| > R_{nucleus}$(radius of the nucleus). Otherwise, it can be expressed by:

$$\vec{F}_i^{\text{nucleus}} = \frac{\vec{r}_i}{|\vec{r}_i|}k_1\text{exp}(k_2(R_{nuc} - |\vec{r}_i|)), \tag{16}$$

where R_{nuc} is the radius of the nucleus.

1.4 Dynein motors

Unfortunately, since the results from the measurements differ greatly, the mechanical properties of dynein remain uncertain. Therefore, the parameters in this section are estimations. The dynein has an anchor and attachment points connected by a stalk. The anchor point has a stable position and the attachment point walks on the MT. The force acting on the MT is determined by the length of the stalk, whose relaxed length was estimates as $L_0 = 18n$m (23–26).

Unattached dynein is represented just with one point on the surface of the cell. If the dynein is closer to the MT than L_0, the motor protein can attach to the filament. Fluctuations of the membrane can move the dynein motor to the MT. Therefore, the attachment probability is defined as:

$$p_a = 5\text{s}^{-1} \qquad d_{md} <= L_0 \tag{17}$$
$$p_a = 5 \cdot \text{exp}(-(d_{md} - L_0)/p_d)\text{s}^{-1} \qquad d_{md} > L_0, \tag{18}$$

where d_{md} is the distance of the dynein point to the closest point of the MT and $p_d = 10^{-7}$ is a chosen parameter. If the MT is attached, the anchor and attachment points of the dynein motor are placed to the same point on the MT. Attachment probability of dynein is unknown; therefore, the attachment probability p_a corresponding to the attachment ratio of kinesin is considered (27). The force of dynein motor comes from the elastic properties of the stalk:

$$|F_i^{\text{Dynein}}| = 0, \qquad |\vec{r}_{\text{Dynein}}| < L_0 \tag{19}$$
$$\vec{F}_i^{\text{Dynein}} = k_{\text{Dynein}}(|\vec{r}_{\text{Dynein}}| - L_0)\frac{\vec{r}_{\text{Dynein}}}{|\vec{r}_{\text{Dynein}}|} \qquad |\vec{r}_{\text{Dynein}}| > L_0, \tag{20}$$

where $\vec{r}_{\text{Dynein}} = \vec{r}_{\text{anchor}} - \vec{r}_{\text{attach}}$ is the distance between the anchor and the attachment points. The measurements of elastic modulus of the stalk differ (28–31) , therefore, the elastic modulus was estimated to $k_{\text{Dynein}} = 400p\text{N}\mu\text{m}^{-1}$ (32). If the force is null or parallel to the preferred direction of stepping, the probability of stepping to the minus end is:

$$p_- = \frac{V_F}{d_{\text{step}}}, \tag{21}$$

where V_F is the forward speed of dynein and d_{step} is the length of the step. The steps of dynein have multiple lengths (33–38). Nevertheless, just the most frequently measured length $d_{\text{step}} = 8\text{nm}$ is considered. The forward speed was estimated or measured in various sources (33, 34, 39–45). For our purposes it is estimated to be $V_F = 1000\text{nms}^{-1}$. In the case of the force of the dynein being in the opposite direction to the preferred movement and smaller than a stall force F_S, the attachment point steps to the minus end with probability:

$$p_- = \frac{V_F}{d_{\text{step}}}(1 - \frac{|F^{\text{Dynein}}|}{F_S}). \tag{22}$$

The value of the stall force varies greatly (33, 33–36, 40, 46) and (47), we estimate it as $F_S = 4\text{pN}$. If the force aims to the plus end and it is bigger than the stall force, dynein steps to the plus end with probability:

$$p_+ = \frac{V_B}{d_{\text{step}}}. \tag{23}$$

Backward stepping speed is force dependent (33) and the measured values also differ (40), (48). Our estimate is $V_B = 6.0\text{nm}\cdot\text{s}^{-1}$ (33).
The probability of detachment is expressed as:

$$p_{\text{detach}} = \exp(\frac{|F_d|}{F_D}), \tag{24}$$

where the detachment force (40, 48, 49) was estimated as $F_D = F_S/2$. When the attachment point of dynein motor is not on a bead of MT, the force is acting on a point of a segment between two beads. In such a case, the force has to be transmitted to the two closest beads. Since the mechanism of stepping and detachment of dynein is uncertain, we use the model for kinesin stepping (50).

Dynein plays a role in two mechanisms. During the cortical sliding mechanism acting in the whole IS, the MT slides on the membrane and its plus-end remains free. MT depolimerizes in the fixed position on the membrane of the cell during capture-shrinkage mechanism acting in the center of the IS. Without the effects of dynein, MT detaches from fixed position.

The densities of capture-shrinkage dyneins, ρ_{IS}, and cortical sliding dynein $\tilde{\rho}_{IS}$ vary through the range that could be expected during the T-Cell activation, $0 < \rho_{IS}, \tilde{\rho}_{IS} < \rho_{\text{MAX}}$. The maximum density of dyneins were estimated considering its structure and size. The dynein comprises a long stalk and a ring-like head containing six AAA+ modules whose diameter is comparable with the length of the stalk (51, 52), and N- and C-terminal regions. The size of the dynein motor can be also estimated from the distance d_{hm} between the head domain of the dynein and the center of the attached MT (53), $d_{\text{hm}} = 28n\text{m}$, which substantially exceeds the length of the dynein stalk. For the case of simplicity, we compute the area of plasma membrane covered by one dynein as $a_{\text{d}} = \pi * L_0^2$, where L_0 is the length of the stalk. The number of dynein N_{dynein} in $1\mu\text{m}^2$ is calculated as

$$N_{\text{dynein}} = \frac{1^{-12}}{a_{\text{d}}} \sim 1000. \tag{25}$$

Consequently, $\rho_{\text{MAX}} = 1000\mu\text{m}^{-2}$.

1.5 Microtubule organizing center (MTOC)

The MTOC is modeled as a planar, polygonal structure, composed from so-called sprouting points(points of MT sprouting). If MTOC has Q^{MTOC} sprouting points, then the equal number of constraints holds them in a specified distance from MTOC center(black lines in Fig. 3). Therefore, the ith constraint is defined as:

$$C_i^{\text{MTOC}} = |\vec{r}_i^{\text{mtoc}} - \vec{r}_c| = R_{\text{MTOC}} \qquad i = 1, ..., Q^{\text{MTOC}}, \tag{26}$$

where $\vec{r}_i^{\text{mtoc}}$ is the position of ith sprouting point and $\vec{r}_c$ is the position of the center of the MTOC. Moreover, additional Q^{MTOC} bonds keep the neighboring points in a constant distance d^{MTOC}(blue lines in Fig. 3).

$$C_i^{\text{MTOC}} = |\vec{r}_i^{\text{mtoc}} - \vec{r}_{i+1}^{\text{mtoc}}| = d^{\text{MTOC}} \qquad i = Q^{\text{MTOC}} + 1, ..., 2 \cdot Q^{\text{MTOC}}, \tag{27}$$

When MT is created, the so-called "sprouting point" and "rear point" on the MTOC are chosen 4. The second bead of the MT is attached to the sprouting point and the first bead to the rear point. Consequently, the original MT orientation is given by the direction from the rear point to the sprouting point. Every MTOC point is the sprouting point to the same number of MTs. The rear point is chosen from the points at the approximately opposite side(relatively to sprouting point) of the MTOC 4a, which gives a variety of the initial MT orientations. Elastic force 4a anchors the MT in the MTOC, while bending force 4b forces the MT to be aligned with the line connecting sprouting and rear points. The combination of two forces assures anchoring of the MT and limitation of changes in orientation, simulating the effect of PCM.

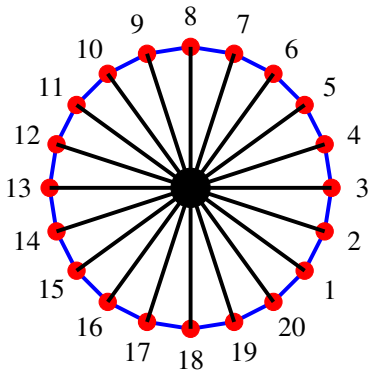

Figure 3: Sketch of the MTOC with $N_{\text{MTOC}} = 20$ MT sprouting points represented by red spheres. The black sphere in the middle depicts the center of the MTOC. Black lines connecting the points with the center and blue lines connecting the neighboring points are nondeformable.

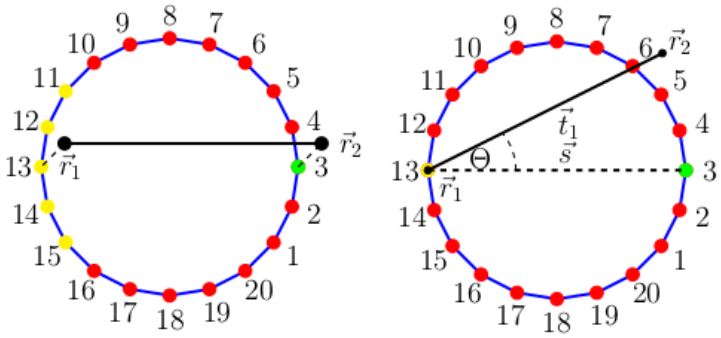

(b) (c)

Figure 4: The sketch of the MTOC and forces connecting the MTOC with MTs. The black line denotes the first segment of microtubule. (a) Dashed lines depict the elastic forces connecting two points of microtubule to two MTOC points. The green point represents the sprouting point and yellow points depict possible rear points. (b) Bending force minimizes the angle Θ between the first segment of microtubule $\vec{t}_1$ and the line $\vec{s}$ connecting sprouting(green) and rear(yellow) point.

1.5.1 Connecting microtubule and MTOC

The first segment of the MT is inside the MTOC 4a. The second and the first the MT beads are attached by elastic forces to the sprouting point and the rear point, respectively 4a. Elastic forces acting on a MT bead can be written as:

$$\vec{F}_2^{\text{elas}} = k_3 |\vec{d}_2| \cdot \frac{\vec{d}_2}{|\vec{d}_2|}, \tag{28}$$

where $k_3 = 30 \cdot \text{pN}\mu\text{m}^{-1}$ is a spring constant and $\vec{d}_2 = \vec{r}_{\text{s}}^{\text{MTOC}} - \vec{r}_2^{\text{micro}}$, where $\vec{r}_{\text{s}}^{\text{MTOC}}$ and $\vec{r}_2^{\text{micro}}$ are MTOC sprouting point and the second bead of MT, respectively. Analogically, we can define the forces between the first bead of the MT and the MTOC rear point. Bending forces 4b are calculated via:

$$\vec{F}_{\text{MTOC}}^{\text{bend}} = \frac{\kappa}{|\vec{s}|^2} \left(-\frac{\vec{t}_1}{|\vec{t}_1|} + \frac{\vec{s}}{|\vec{s}|} \left(\frac{\vec{t}_1 \cdot \vec{s}}{|\vec{s}||\vec{t}_1|} \right) \right) \tag{29a}$$

$$\vec{F}_{\text{micro}}^{\text{bend}} = \frac{\kappa}{|\vec{t}_1|^2} \left(\frac{\vec{s}}{|\vec{s}|} - \frac{\vec{t}_1}{|\vec{t}_1|} \left(\frac{\vec{t}_1 \cdot \vec{s}}{|\vec{s}||\vec{t}_1|} \right) \right), \tag{29b}$$

$$\vec{F}_0 = -\vec{F}_{\text{micro}}^{\text{bend}} - \vec{F}_{\text{MTOC}}^{\text{bend}} \tag{29c}$$

where $\vec{s}$ is the segment between the two beads of the MTOC, $\vec{t}_1$ is the first segment of MT. The forces $\vec{F}_{\text{MTOC}}^{\text{bend}}$ and $\vec{F}_{\text{micro}}^{\text{bend}}$ act on the sprouting point and the second bead of MT, respectively. The force $\vec{F}_0$ acts on the first bead of the MT and the rear point.

2 Constrained Langevin dynamics

Using Langevin dynamics, the motion of an unconstrained particle with the position x_i can be expressed:

$$\gamma_i \dot{x}_i = f_i + \eta_i, \tag{30}$$

where η_i is a random Langevin force, which is a stochastic, non-differentiable function of time that integrates random interactions with the molecules of the solvent. The force f_i is the sum of all other forces and it depends on the object and γ is the drag coefficient. In a constrained case, N beads in 3D have to satisfy Q constraints (54):

$$C_a(x_1, ..., x_{3*N}) = c_a \qquad a = 1, ..., Q \tag{31}$$

The constraints have to remain constant in every instance. Therefore, the movement of the beads must satisfy:

$$0 = \dot{C}_a = n_{ia} \cdot \dot{x}_i \qquad a = 1, ..., Q \tag{32}$$

where

$$n_{ia} = \frac{\partial C_a}{\partial x_i}. \tag{33}$$

The motion of a constrained bead can be expressed:

$$\gamma \dot{x}_i = f_i + \eta_i - n_{ia}\lambda_a, \tag{34}$$

where λ_a is the constraint force conjugate to the constraint μ.

2.1 Mid-Step algorithm

Mid-Step algorithm was proposed by Fixman and further generalized by Hinch and Grassia (55–58) The algorithms was elaborated for specific cases by Morse and Pasquali (54) and (59). Using the mobility tensor

$$H_{ik}\gamma = \mathbf{I}_{ik}, \tag{35}$$

the equation (34) can be rewritten as:

$$\dot{x}_i = H_{ij}[F_j^u - n_{ja}\lambda_a], \tag{36}$$

where $F_j^u = f_i + \eta_i$ is unconstrained force. The values of λ_a for $a = 1, ..., Q$ can be calculated from the conditions (32) at every instant. It will result in the set of algebraic equations:

$$G_{a\nu}\lambda_\nu = n_{ia}H_{ij}F_j^u, \tag{37}$$

where

$$G_{a\nu} = n_{ia}H_{ij}n_{j\nu}. \tag{38}$$

If the constraint forces are expressed by (37), we get the equation of motion from (34):

$$\dot{x}_i = P_{ij}H_{jk}F_k^u, \tag{39}$$

where

$$P_{ij} = \mathbf{I}_{ij} - H_{ik}n_{ka}G^{-1}_{a\nu}n_{j\nu} \tag{40}$$

is a projection operator. In the case when the mobility tensor is expressed by (35), equation 40 can be rewritten as:

$$P_{ij} = \mathbf{I}_{ij} - n_{ia}T^{-1}_{a\nu}n_{j\nu}, \tag{41}$$

where

$$T_{a\nu} = n_{ia}n_{i\nu}. \tag{42}$$

The dynamical projection operator is used to project forces to $3N - Q$ dimensional hypersurface. Therefore, they are locally perpendicular to the constraints.

The mid-step algorithm proposed by Hinch is for the case of mobility tensor (35) composed by four following substeps:

1. Generate unprojected random forces η_i and unprojected forces f_i at initial position x_i^0;
2. Construct projected random force $\eta_i^P = P_{ij}\eta_j$ and $f_i^P = P_{ij}f_j$;
3. Calculate midstep position $x_i^{1/2} = x_i^0 + \dot{x}_i^0\Delta t/2$, where the mobility in the original configuration $\dot{x}_i^0$ is calculated via (39) and Δt is the time step;
4. Calculate updated bead positions $x_i^1 = x_i^0 + \dot{x}_i^{1/2}\Delta t$, where $\dot{x}_i^{1/2}$ is evaluated with the deterministic and normal vectors from mid position, but with the same projected random force from initial configuration.

Mid-step algorithm uses the projection operator (40) that alongside with the mid position calculation minimizes the perturbations of constraints. Nevertheless, perturbations cannot be eliminated. Therefore, the MT has to be resized to fulfill the constraints. In such operation, the angles between $\vec{t}_i$ and $\vec{t}_{i+1}$, where $i = 1, ..., N-1$ are conserved, the first bead of MT remains constant and MT regrows from the MTOC. Consequently, the bending energy of the MT remains unchanged.

3 Additional results

3.1 Influence of random forces

Random forces acting on the MTs have small effects since the motion of the MTs is constrained. Fig. 5a suggests that random forces perpendicular to the cell membrane(red) have no effect since microtubule curvature is given by the interplay of bending forces and the force of the membrane. The green forces, acting parallel to the segments of the MTs have also no impact, because the MT is attached to the MTOC, making it a part of a very massive structure. Consequently, just random forces depicted in purple in 5b can result in movement, making the random noise effectively one-dimensional. However, the MT is still rigid structure, random forces act in contradiction and filament is bound to MTOC, which seriously limits the movement of upper beads. Therefore, the influence of random noise can be expected to be negligible. Moreover, the capture-shrinkage mechanism fixates the MT on both sides, further minimizing the effect of the random force. In Figs. 6a and 6b we can see that the repositioning curves are almost identical for the case of the capture-shrinkage mechanism. The Figs. 6c and 6d demonstrate that the developments of the number of attached dyneins also do not differ. During cortical sliding repositionings the effect of the random forces is also negligible 7.

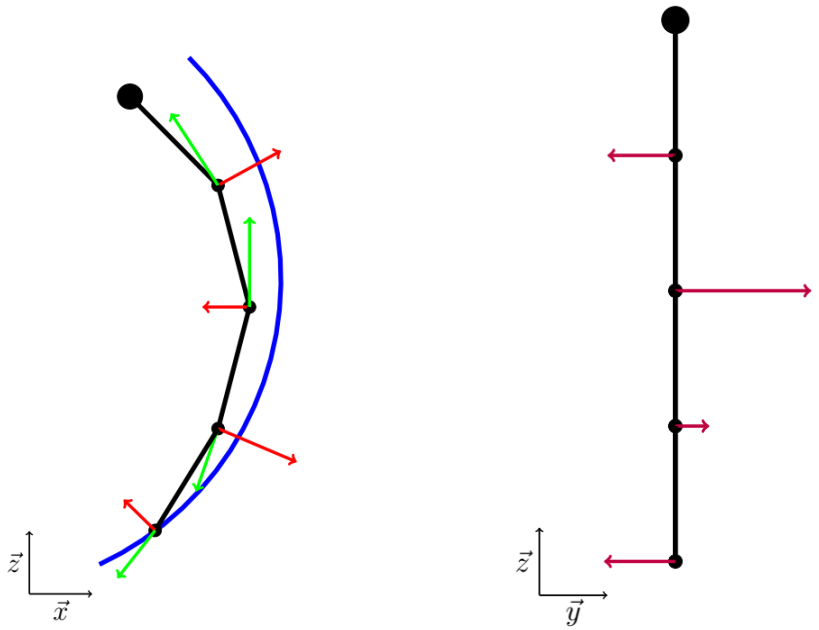

(a) (b)

Figure 5: Sketch of random forces acting on the MT from two perspectives. The big circle represents MTOC and smaller circles represent beads of microtubule. Blue arc depicts membrane of the cell. Red, green and purple lines representing random forces acting on every bead are perpendicular.

3.2 Comparison of two cases with different number of microtubules

The cytoskeleton of $M_{\text{micro}} = 100$ MTs (examined in previous section) is compared with the cytoskeleton of $M_{\text{micro}} = 40$. We define $n_{\text{dm}}(t) = \frac{\bar{N}_{\text{dm}}(t)}{M_{\text{micro}}}$ to examine the ratio of the attached dyneins and the number of the MTs in a cytoskeleton. Fig. 8a depicts repolarization curves of two cytoskeletons for the case of the capture-shrinkage mechanism. The polarization exhibits a triphasic behavior for both cases 8b.

We define $n_{\text{max}} = \max(n_{\text{dm}}(t))$. In Figs 8c it can be seen that n_{max} is always bigger for the case of smaller cytoskeleton(caused by the small area of the center of IS and limited number of dynein). The Figs. 8c and 8d explain the differences of speed in terms of the number of motors. When the area density is small, the smaller cytoskeleton is pulled with relatively higher force. As the concentration increases, the maximum speed is achieved($\rho_{\text{IS}} \sim 600\mu\text{m}^{-2}$). Subsequent increase of pulling force has no effect.

Figs. 9a and 9b depicting the repositioning under the influence of the cortical sliding mechanism shows the three regimes for both cytoskeletons. In both cases, n_{max} rises at the beginning, it reaches its maximum when $\tilde{\rho}_{\text{IS}} \sim 200\mu\text{m}^{-2}$ and then it decreases swiftly and then steadily 9c. For smaller densities, the number of dyneins per MT are smaller for the bigger cytoskeleton. The situation is opposite when considering high area densities. Since the attached MTs aim in different directions, dyneins compete in the area of higher densities. As the number of the MT decreases, the pulling forces acting on individual filaments increase, leading to faster detachment. The MTOC speed increases when $\tilde{\rho}_{\text{IS}} < 200\mu\text{m}^{-2}$ and then it decreases. We can see in 9d that the speed decreases for both cases even when n_{max} stays approximately the same, which is the consequence of dynein acting predominantly at the periphery.

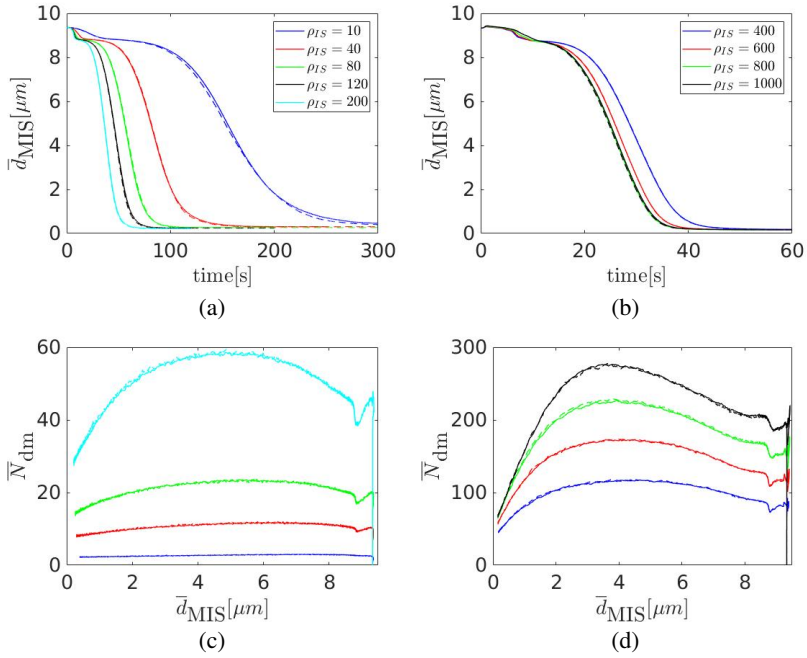

Figure 6: Combination of the capture-shrinkage mechanism and random forces. Solid lines stand for the sole capture shrinkage and dashed lines for the combination with random forces. Legends in (a), (b) apply for (c), (d), respectively. (a)(b) Dependence of the average MTOC-IS distance $\bar{d}_{\mathrm{MIS}}$ on time, (c)(d) Dependence of the average number of dynein $\bar{N}_{\mathrm{dm}}$ motors on MTOC-IS distance $\bar{d}_{\mathrm{MIS}}$.

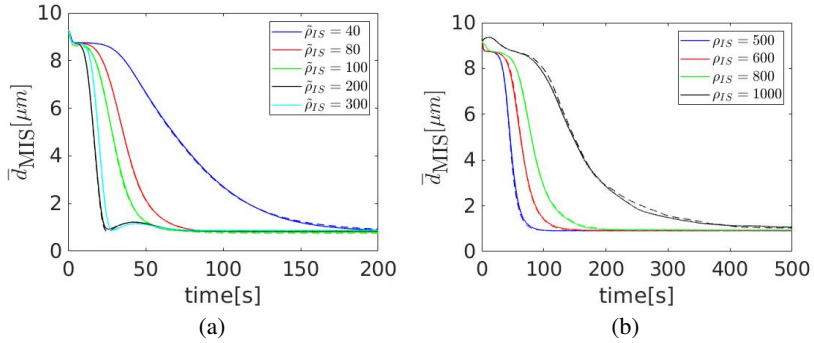

Figure 7: Combination of the cortical sliding mechanism and random forces. Solid lines stand for the sole cortical sliding and dashed lines for the combination with random forces. (a)(b) Dependence of the average MTOC-IS distance $\bar{d}_{\mathrm{MIS}}$ on time.

3.3 Capture-shrinkage and cortical sliding combined

As can be seen in Fig. 10b, addition of the small area density of capture-shrinkage dyneins in the center of IS causes substantial decrease of differences between times of polarization. Moreover, the three regimes of behavior based on the area density of cortical sliding dyneins is not observed in the presence of the capture-shrinkage mechanism. Surely, the third regime presents a disadvantage, since the pulling force of dynein is wasted in unproductive competitions. Therefore, the synergy of two mechanisms proves once more to be highly effective, since it does not only removes the third regime, but also greatly reduces the times of repositioning when the area density of cortical sliding $\tilde{\rho}_{\mathrm{IS}} < 100\mu\mathrm{m}^{-2}$. Fig. 10a depicts times of repositioning for different sets of combined mechanisms since the capture-shrinkage area density varies and cortical sliding density remains constant. We can see that the times of repositioning are in general shorter for the case of combined mechanisms. Moreover, even when the area densities correspond to the second regime, the times of repositioning are comparable. Combined cases, however, have just 15% of the number of dyneins. Additionally, we can notice that the increase of area densities when $\tilde{\rho}_{\mathrm{IS}} > 500\mu\mathrm{m}^{-2}$ presents no advantage since it causes slowing down of repositioning in the absence of capture-shrinkage and has no effect when the mechanisms are combined. Fig. 10c shows that the attached dyneins are predominantly located on the periphery of IS even in the case when $\tilde{\rho}_{\mathrm{IS}} > \rho_{\mathrm{IS}}$.

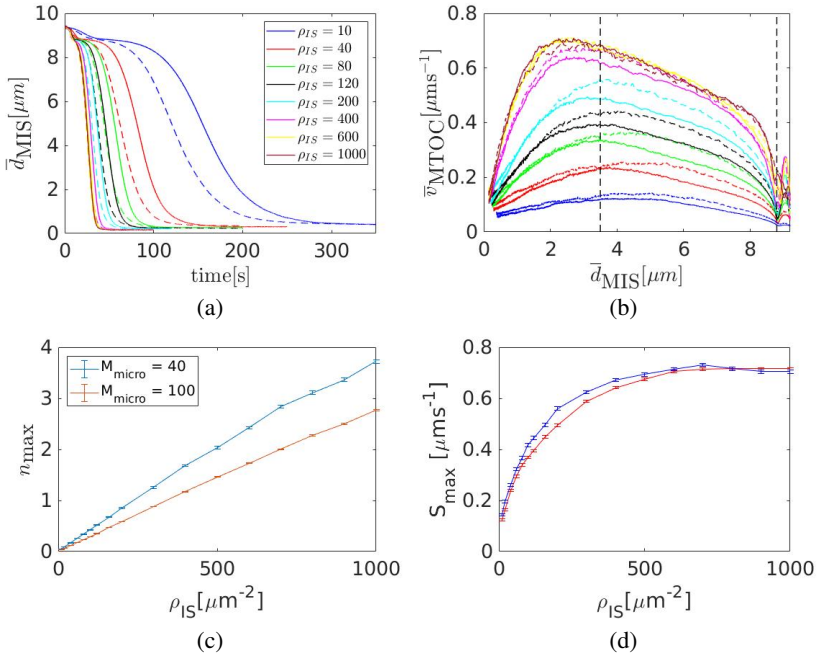

Figure 8: Capture-shrinkage mechanism for two cytoskeletons with different numbers of microtubules: $M_{\mathrm{micro}} = 100$(solid lines) and $M_{\mathrm{micro}} = 40$(dashed lines). (a) Dependence of average MTOC-IS distance $\bar{d}_{\mathrm{MIS}}$ on time. (b) Dependence of average MTOC speed $\bar{v}_{\mathrm{MTOC}}$ on $\bar{d}_{\mathrm{MIS}}$. (c) Dependence of the maximum number of attached dyneins per microtubule $n_{\max}$ on area density ρ_{IS}. (d) Dependence of the maximum speed $S_{\max}$ on ρ_{IS}.

4 Commentary on modeling approaches

4.1 Cytosim

Cytosim is widely accepted as an efficient tool for the simulations of fibers (60). Although there are many similarities between the models, we decided not to use Cytosim. The first reason is our goal to examine the role of Brownian motion. The implicit integration used by Cytosim has a numerical error that could influence the precision of calculation in the absence of thermal noise. The second reason is the simplified calculation of the bending forces used by Cytosim. The advantage of such an approach, which enables to express the bending forces as a result of a matrix-vector multiplication, is a great efficiency of calculation. Nevertheless, the procedure is valid only if the angles between subsequent segments remain small. This presents a drawback, since the angles between the segment increase as the radius of the cell decrease. More importantly, substantial curvature of the MTs can be expected during repositioning (61)(See 4.4). Moreover, the "reshaping" of the objects due to the numerical impressions is done to keep the center of mass constant. Since the rigidity of MTOC is an important part of our model, reshaping is done to keep the first the bead of the MT(therefore MTOC-MT forces) constant.

4.2 Model using deterministic force

Kim and Maly (62) modeled the cortical sliding mechanism using the deterministic force. Although this model has various merits, it leads to the contradiction with some experimental observable: for example MTs stalk going through the center (62). This presents a drawback since various biological functions depend on the distribution of MTs.

References

1. Broedersz, C., and F. MacKintosh, 2014. Modeling semiflexible polymer networks. *Rev. Mod. Phys.* 86:995–1036.

2. Puchkov, E. O., 2013. Intracellular viscosity: Methods of measurement and role in metabolism. *Biochem. Moscow Suppl. Ser. A* 7:270–279.

3. Bausch, A. R., W. Möller, and E. Sackmann, 1999. Measurement of local viscoelasticity and forces in living cells by magnetic tweezers. *Biophys J* 76:573–579.

4. Howard, J., 2001. Mechanics of Motor Proteins and the Cytoskeleton. Sinauer Associates is an imprint of Oxford University Press, Sunderland, Mass, new edition.

5. Leith, D., 1987. Drag on Nonspherical Objects. *Aerosol Science and Technology* 6:153–161.

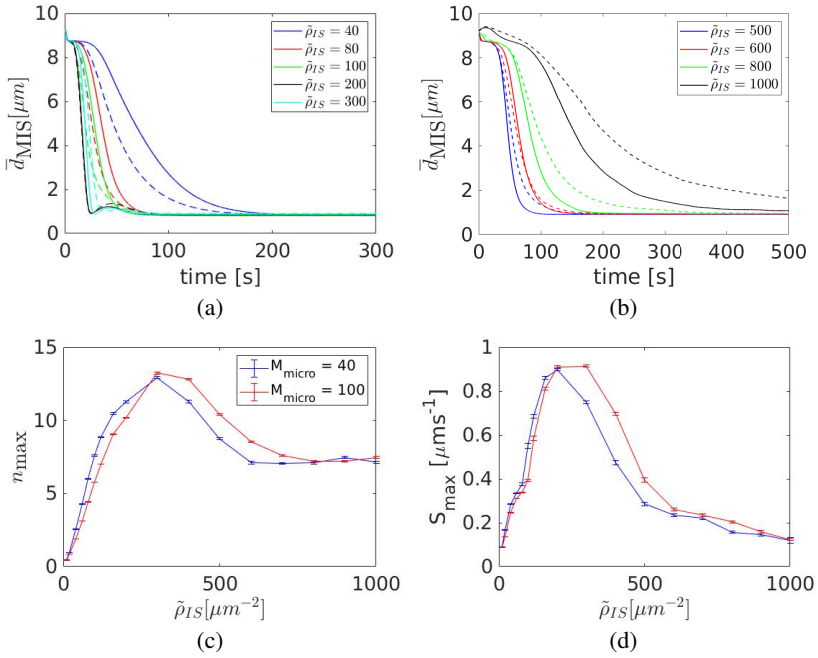

Figure 9: Cortical sliding mechanism for two cytoskeletons with different numbers of microtubules $M_{\text{micro}} = 100$(solid lines) and $M_{\text{micro}} = 40$(dashed lines). (a)(b) Dependence of average MTOC-IS distance $\bar{d}_{\text{MIS}}$ on time. (c) Dependence of the number of attached dyneins per microtubule n_{max} on the area density $\tilde{\rho}_{\text{IS}}$. (d) Dependence of the maximum speed S_{max} on $\tilde{\rho}_{\text{IS}}$.

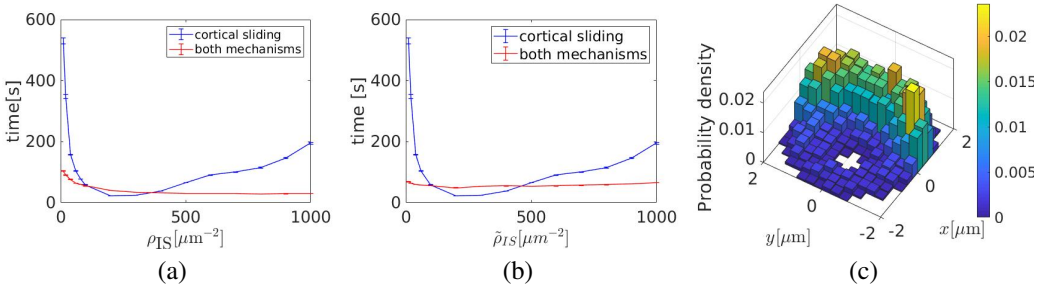

Figure 10: Combination of the capture-shrinkage and the cortical sliding mechanisms. (a)(b) Times of repositioning for the sole cortical sliding and combinations of two mechanisms. (a)In the combined case the capture-shrinkage area density varies, cortical sliding area density is constant $\tilde{\rho}_{\text{IS}} = 20\mu\text{m}^{-2}$. (b)In the combined case the cortical sliding area density $\tilde{\rho}_{\text{IS}}$ varies and capture-shrinkage area density is constant $\rho_{\text{IS}} = 60\mu\text{m}^{-2}$. (c) Two dimensional probability density of attached dynein $\tilde{\rho}_{\text{IS}} = 60\mu\text{m}^{-2}$, $\rho_{\text{IS}} = 20\mu\text{m}^{-2}$, $\bar{d}_{MIS} = 4.5\mu$m.

6. Maccari, I., R. Zhao, M. Peglow, K. Schwarz, I. Hornak, M. Pasche, A. Quintana, M. Hoth, B. Qu, and H. Rieger, 2016. Cytoskeleton rotation relocates mitochondria to the immunological synapse and increases calcium signals. *Cell Calcium* 60:309–321.

7. Bereiter-Hahn, J., and M. Vöth, 1994. Dynamics of mitochondria in living cells: shape changes, dislocations, fusion, and fission of mitochondria. *Microsc. Res. Tech.* 27:198–219.

8. Jakobs, S., 2006. High resolution imaging of live mitochondria. *Biochimica et Biophysica Acta (BBA) - Molecular Cell Research* 1763:561–575.

9. Chaudhuri, A., 2016. Cell Biology by the Numbers. *Yale J Biol Med* 89:425–426.

10. 1966. An Atlas of Fine Structure. The Cell. Its Organelles and Inclusions. *Ann Intern Med* 64:968.

11. Jakobs, S., and C. A. Wurm, 2014. Super-resolution microscopy of mitochondria. *Current Opinion in Chemical Biology* 20:9–15.

12. Xu, H., W. Su, M. Cai, J. Jiang, X. Zeng, and H. Wang, 2013. The Asymmetrical Structure of Golgi Apparatus Membranes Revealed by In situ Atomic Force Microscope. *PLoS One* 8.

13. Ladinsky, M. S., D. N. Mastronarde, J. R. McIntosh, K. E. Howell, and L. A. Staehelin, 1999. Golgi Structure in Three Dimensions: Functional Insights from the Normal Rat Kidney Cell. *J Cell Biol* 144:1135–1149.

14. Day, K. J., L. A. Staehelin, and B. S. Glick, 2013. A Three-Stage Model of Golgi Structure and Function. *Histochem Cell Biol* 140:239–249.

15. Huang, S., and Y. Wang, 2017. Golgi structure formation, function, and post-translational modifications in mammalian cells. *F1000Res* 6.

16. Westrate, L. M., J. E. Lee, W. A. Prinz, and G. K. Voeltz, 2015. Form follows function: the importance of endoplasmic reticulum shape. *Annu. Rev. Biochem.* 84:791–811.

17. English, A. R., and G. K. Voeltz, 2013. Endoplasmic reticulum structure and interconnections with other organelles. *Cold Spring Harb Perspect Biol* 5:a013227.

18. English, A. R., N. Zurek, and G. K. Voeltz, 2009. Peripheral ER structure and function. *Curr. Opin. Cell Biol.* 21:596–602.

19. Shibata, Y., G. K. Voeltz, and T. A. Rapoport, 2006. Rough sheets and smooth tubules. *Cell* 126:435–439.

20. Hu, J., W. A. Prinz, and T. A. Rapoport, 2011. Weaving the Web of ER Tubules. *Cell* 147:1226–1231.

21. Gurel, P., A. Hatch, and H. Higgs, 2014. Connecting the Cytoskeleton to the Endoplasmic Reticulum and Golgi. *Current Biology* 24:R660–R672.

22. Alberts, B., A. Johnson, J. Lewis, M. Raff, K. Roberts, and P. Walter, 2007. Molecular Biology of the Cell, 5th Edition. Garland Science, New York, 5th edition edition.

23. Goodenough, U. W., B. Gebhart, V. Mermall, D. R. Mitchell, and J. E. Heuser, 1987. High-pressure liquid chromatography fractionation of Chlamydomonas dynein extracts and characterization of inner-arm dynein subunits. *Journal of Molecular Biology* 194:481–494.

24. Gee, M. A., J. E. Heuser, and R. B. Vallee, 1997. An extended microtubule-binding structure within the dynein motor domain. *Nature* 390:636–639.

25. Goodenough, U., and J. Heuser, 1984. Structural comparison of purified dynein proteins with in situ dynein arms. *Journal of Molecular Biology* 180:1083–1118.

26. Schmidt, H., E. S. Gleave, and A. P. Carter, 2012. Insights into dynein motor domain function from a 3.3 Å crystal structure. *Nat Struct Mol Biol* 19:492–S1.

27. Leduc, C., O. Campàs, K. B. Zeldovich, A. Roux, P. Jolimaitre, L. Bourel-Bonnet, B. Goud, J.-F. Joanny, P. Bassereau, and J. Prost, 2004. Cooperative extraction of membrane nanotubes by molecular motors. *Proc. Natl. Acad. Sci. U.S.A.* 101:17096–17101.

28. Kamiya, N., T. Mashimo, Y. Takano, T. Kon, G. Kurisu, and H. Nakamura, 2016. Elastic properties of dynein motor domain obtained from all-atom molecular dynamics simulations. *Protein Eng Des Sel* 29:317–325.

29. Burgess, S. A., M. L. Walker, H. Sakakibara, P. J. Knight, and K. Oiwa, 2003. Dynein structure and power stroke. *Nature* 421:715–718.

30. Lindemann, C. B., and A. J. Hunt, 2003. Does axonemal dynein push, pull, or oscillate? *Cell Motil. Cytoskeleton* 56:237–244.

31. Sakakibara, H., H. Kojima, Y. Sakai, E. Katayama, and K. Oiwa, 1999. Inner-arm dynein c of Chlamydomonas flagella is a single-headed processive motor. *Nature* 400:586–590.

32. Sakakibara, H., and K. Oiwa, 2011. Molecular organization and force-generating mechanism of dynein. *The FEBS Journal* 278:2964–2979.

33. Gennerich, A., A. P. Carter, S. L. Reck-Peterson, and R. D. Vale, 2007. Force-Induced Bidirectional Stepping of Cytoplasmic Dynein. *Cell* 131:952–965.

34. Toba, S., T. M. Watanabe, L. Yamaguchi-Okimoto, Y. Y. Toyoshima, and H. Higuchi, 2006. Overlapping hand-over-hand mechanism of single molecular motility of cytoplasmic dynein. *PNAS* 103:5741–5745.

35. Mallik, R., D. Petrov, S. A. Lex, S. J. King, and S. P. Gross, 2005. Building complexity: an in vitro study of cytoplasmic dynein with in vivo implications. *Curr. Biol.* 15:2075–2085.

36. Mallik, R., B. C. Carter, S. A. Lex, S. J. King, and S. P. Gross, 2004. Cytoplasmic dynein functions as a gear in response to load. *Nature* 427:649–652.

37. Reck-Peterson, S. L., A. Yildiz, A. P. Carter, A. Gennerich, N. Zhang, and R. D. Vale, 2006. Single-Molecule Analysis of Dynein Processivity and Stepping Behavior. *Cell* 126:335–348.

38. Kural, C., H. Kim, S. Syed, G. Goshima, V. I. Gelfand, and P. R. Selvin, 2005. Kinesin and dynein move a peroxisome in vivo: a tug-of-war or coordinated movement? *Science* 308:1469–1472.

39. Torisawa, T., M. Ichikawa, A. Furuta, K. Saito, K. Oiwa, H. Kojima, Y. Y. Toyoshima, and K. Furuta, 2014. Autoinhibition and cooperative activation mechanisms of cytoplasmic dynein. *Nature Cell Biology* 16:1118–1124.

40. Müller, M. J. I., S. Klumpp, and R. Lipowsky, 2008. Tug-of-war as a cooperative mechanism for bidirectional cargo transport by molecular motors. *Proc. Natl. Acad. Sci. U.S.A.* 105:4609–4614.

41. King, S. J., and T. A. Schroer, 2000. Dynactin increases the processivity of the cytoplasmic dynein motor. *Nat Cell Biol* 2:20–24.

42. Nishiura, M., T. Kon, K. Shiroguchi, R. Ohkura, T. Shima, Y. Y. Toyoshima, and K. Sutoh, 2004. A single-headed recombinant fragment of Dictyostelium cytoplasmic dynein can drive the robust sliding of microtubules. *J. Biol. Chem.* 279:22799–22802.

43. Kon, T., M. Nishiura, R. Ohkura, Y. Y. Toyoshima, and K. Sutoh, 2004. Distinct Functions of Nucleotide-Binding/Hydrolysis Sites in the Four AAA Modules of Cytoplasmic Dynein. *Biochemistry* 43:11266–11274.

44. Cho, C., S. L. Reck-Peterson, and R. D. Vale, 2008. Regulatory ATPase sites of cytoplasmic dynein affect processivity and force generation. *J. Biol. Chem.* 283:25839–25845.

45. Kikushima, K., T. Yagi, and R. Kamiya, 2004. Slow ADP-dependent acceleration of microtubule translocation produced by an axonemal dynein. *FEBS Letters* 563:119–122.

46. Walter, W. J., B. Brenner, and W. Steffen, 2010. Cytoplasmic dynein is not a conventional processive motor. *J. Struct. Biol.* 170:266–269.

47. Belyy, V., M. A. Schlager, H. Foster, A. E. Reimer, A. P. Carter, and A. Yildiz, 2016. The mammalian dynein-dynactin complex is a strong opponent to kinesin in a tug-of-war competition. *Nat. Cell Biol.* 18:1018–1024.

48. Ikuta, J., N. K. Kamisetty, H. Shintaku, H. Kotera, T. Kon, and R. Yokokawa, 2014. Tug-of-war of microtubule filaments at the boundary of a kinesin- and dynein-patterned surface. *Scientific Reports* 4:5281.

49. Kunwar, A., S. K. Tripathy, J. Xu, M. K. Mattson, P. Anand, R. Sigua, M. Vershinin, R. J. McKenney, C. C. Yu, A. Mogilner, and S. P. Gross, 2011. Mechanical stochastic tug-of-war models cannot explain bidirectional lipid-droplet transport. *Proc. Natl. Acad. Sci. U.S.A.* 108:18960–18965.

50. Klein, S., C. Appert-Rolland, and L. Santen, 2015. Motility states in bidirectional cargo transport. *EPL* 111:68005.

51. Roberts, A. J., N. Numata, M. L. Walker, Y. S. Kato, B. Malkova, T. Kon, R. Ohkura, F. Arisaka, P. J. Knight, K. Sutoh, and S. A. Burgess, 2009. AAA+ Ring and Linker Swing Mechanism in the Dynein Motor. *Cell* 136:485–495.

52. Imai, H., T. Shima, K. Sutoh, M. L. Walker, P. J. Knight, T. Kon, and S. A. Burgess, 2015. Direct observation shows superposition and large scale flexibility within cytoplasmic dynein motors moving along microtubules. *Nature Communications* 6:1–11.

53. Mizuno, N., A. Narita, T. Kon, K. Sutoh, and M. Kikkawa, 2007. Three-dimensional structure of cytoplasmic dynein bound to microtubules. *PNAS* 104:20832–20837.

54. Montesi, A., D. C. Morse, and M. Pasquali, 2005. Brownian dynamics algorithm for bead-rod semiflexible chain with anisotropic friction. *J. Chem. Phys.* 122:084903.

55. Fixman, M., 1978. Simulation of polymer dynamics. I. General theory. *J. Chem. Phys.* 69:1527–1537.

56. Hinch, E. J., 1994. Brownian motion with stiff bonds and rigid constraints. *Journal of Fluid Mechanics* 271:219–234.

57. Grassia, P. S., E. J. Hinch, and L. C. Nitsche, 1995. Computer simulations of Brownian motion of complex systems. *Journal of Fluid Mechanics* 282:373–403.

58. Grassia, P., and E. J. Hinch, 1996. Computer simulations of polymer chain relaxation via Brownian motion. *Journal of Fluid Mechanics* 308:255–288.

59. Pasquali, M., and D. C. Morse, 2002. An efficient algorithm for metric correction forces in simulations of linear polymers with constrained bond lengths. *The Journal of Chemical Physics* 116:1834–1838.

60. Nedelec, F., and D. Foethke, 2007. Collective Langevin dynamics of flexible cytoskeletal fibers. *New J. Phys.* 9:427–427.

61. Kuhn, J. R., and M. Poenie, 2002. Dynamic Polarization of the Microtubule Cytoskeleton during CTL-Mediated Killing. *Immunity* 16:111–121.

62. Kim, M. J., and I. V. Maly, 2009. Deterministic Mechanical Model of T-Killer Cell Polarization Reproduces the Wandering of Aim between Simultaneously Engaged Targets. *PLOS Computational Biology* 5:e1000260.